FRIEDRICH-ALEXANDER-UNIVERSITÄT ERLANGEN-NÜRNBERG
INSTITUT FÜR INFORMATIK (MATHEMATISCHE MASCHINEN UND DATENVERARBEITUNG)

Lehrstuhl für Informatik 10 (Systemsimulation)

Special Finite Elements for Dipole Modelling

Martin Bauer

Master Thesis

Special Finite Elements for Dipole Modelling

Martin Bauer

Master Thesis

Erlangen, den 3.3.2012

Aufgabensteller: Prof. Dr. U. Rüde
Betreuer: H. Köstler

Erklärung:

Ich versichere, dass ich die Arbeit ohne fremde Hilfe und ohne Benutzung anderer als der angegebenen Quellen angefertigt habe und dass die Arbeit in gleicher oder ähnlicher Form noch keiner anderen Prüfungsbehörde vorgelegen hat und von dieser als Teil einer Prüfungsleistung angenommen wurde. Alle Ausführungen, die wörtlich oder sinngemäß übernommen wurden, sind als solche gekennzeichnet.

Erlangen, den .....

Abstract

This thesis focuses on the solution of the EEG forward problem, using the finite element method. The goal is to compare different dipole models for a current source in the human head, with a focus on Whitney type basis functions. For the current sources in the head a widely used model is the mathematical or current dipole. Its strong singularity poses a problem for numerical methods. Therefore we investigate a less singular dipole model based on Whitney forms. In the first part of the thesis we give an overview of the EEG forward problem and the theory behind Whitney elements. Then we investigate methods for representing a mathematical dipole in Whitney formulation, in order to validate the Whitney approach. The following comparison of the available models on tetrahedral and hexahedral meshes shows, that the Whitney model achieves the highest accuracy if the local mesh geometry can represent the dipole moment well. Otherwise interpolation techniques have to be used, which worsen the accuracy, making the Whitney approach inferior to the other methods in the general case.

Contents

1 Introduction

The human brain is one of the most interesting human organs and at the same time one of the least understood. We know its structure and its working mechanism on a low level, for example the mechanism of signal transfer, but how this leads to more complex concepts like emotions or memories is still beyond our understanding.
A big step forward in the field of brain research, was made by the German physiologist and psychiatrist Hans Berger in 1924: He recorded the first human electroencephalogram (EEG). He placed electrodes on the surface of the head to measure the electric field, generated by activated brain regions. By just analyzing the frequency range of these measurements one can already determine so called wave patterns that are indicators for a certain state of mind. There are typical wave patterns for sleep, drowsiness, movement or active concentration. This makes the EEG a valuable tool in the area of sleep research.
Another important application field of the EEG is epilepsy diagnose and treatment. In focal epilepsy a seizure is caused by a pathological neuronal activity that spreads out to large portions of the brain, disturbing sensomotoric functions and thus leading to symptoms of an epileptic seizure. An EEG measurement that was recorded during a seizure is depicted in Fig. 1.1. The seizure manifests itself in the EEG in the sudden change of waveforms, and the occurrences of so called spikes. EEG measurements can not only help to diagnose epilepsy but also to determine the location of the pathological brain region that caused the seizure. This localization opens the possibility of a resective surgery, where the defective brain tissue is removed.

Figure 1.1 – EEG during an epileptic seizure
Source: Wikimedia Commons

The localization of currents inside the brain, based on EEG measurements, the so called *EEG inverse problem*, is a mathematically ill-posed problem [KS05, PM99]. Ill-posedness is defined by the negation of its counterpart, called well-posedness. A mathematically well-posed problem as defined by Hadamard is required to have a unique solution, and this solution has to depend continuously on the input data. The last condition is important, since otherwise small perturbations in the input data can lead to arbitrary big errors in the solution. These perturbations can be caused by measurement inaccuracies or parameter uncertainties.
The EEG inverse problem is not well posed in the sense described above. One reason is, that it does not possess a unique solution. For a given potential there are infinitely many source configurations that lead to this potential. Another reason is the violation of the last condition: The resulting source configuration does not depend continuously on the EEG input signal, which means that in principle noise in the EEG data may lead to solutions that are arbitrarily

far away from the real solution.
In order to solve the inverse problem despite its ill-posedness, one has to use regularization methods that utilize additional information about the problem. A typical assumption is, that the field is generated by a fixed number of dipoles.
All inverse methods need to compute several solutions to the forward problem. They test how well the field of an assumed source configuration fits the measured field, and change the source parameters accordingly, to get a good match between both fields. Therefore it is crucial to have a fast and exact solver for the forward problem available.
For solving the EEG forward problem numerically one can choose between the boundary element method (BEM) and the finite element method (FEM). In this thesis we will focus on the finite element method since it is the most flexible but also the computationally most intensive method. For a detailed comparison of both methods see [Vor11]. When using the finite element method one has to find a way to map the strongly singular mathematical dipole source model, that is used to model currents in the brain, to the discrete setting. Several models have been developed to do this, which all try to treat the singularity of the mathematical dipole as exact as possible in the numerical method.
The task of this thesis is to implement and investigate a new type of source model that uses so called Whitney ansatz functions. The Whitney dipole model does not try to map the mathematical dipole to the discrete domain, but instead represents directly a source of small extend on a finite domain.
In Chapter 2 we will first give a short overview of the physiological background, then continue with the mathematical formulation of the EEG forward problem in its continuous and discrete version, and conclude with an overview of the established source models. The following chapter deals with the mathematical discipline of differential geometry where Whitney forms have their theoretical basis. In Chapter 4 we derive a formulation of Whitney forms suitable to be used in the finite element method. Then we run numerical tests to evaluate the accuracy and performance of each source model (Chapter 5).

2 The EEG Forward Problem

In this chapter we introduce the EEG forward problem. We start by describing its physiological origins, then continue deriving the mathematical formulation based on Maxwell's equations. We conclude this chapter by giving a finite element formulation of the problem and presenting three established source models which can be used to model a current dipole in the finite element method.

2.1 Physiological Background

The electrical activity inside the brain consists out of currents, generated by single nervous cells (neurons). There are about 10^{10} single neurons in the human brain, which are interconnected by approximately 10^{14} synapses.
Although neurons can greatly vary in size, they all have the same structure. Every neuron consists out of three parts: The *dendrites* are branched out structures, responsible for collecting electrochemical stimulations from other neurons. They are connected to the cell body, the *soma* which acts as an adder and amplifier for received signals. From there the signal goes on to the *axon* which is connected to other neurons via *synapses* that perform the electrochemical signalling between two neurons.
The energy needed for this signal transmission is generated by a chemical process called the *sodium-potassium pump*. This process pumps Na^+ ions out of the cell and K^+ ions to the inside, resulting in a high concentration of sodium ions in the extracellular region, and a high potassium concentration on the inside. Since this process works against the concentration and potential gradient, it needs energy which is supplied in form of ATP (adenosine triphosphate).

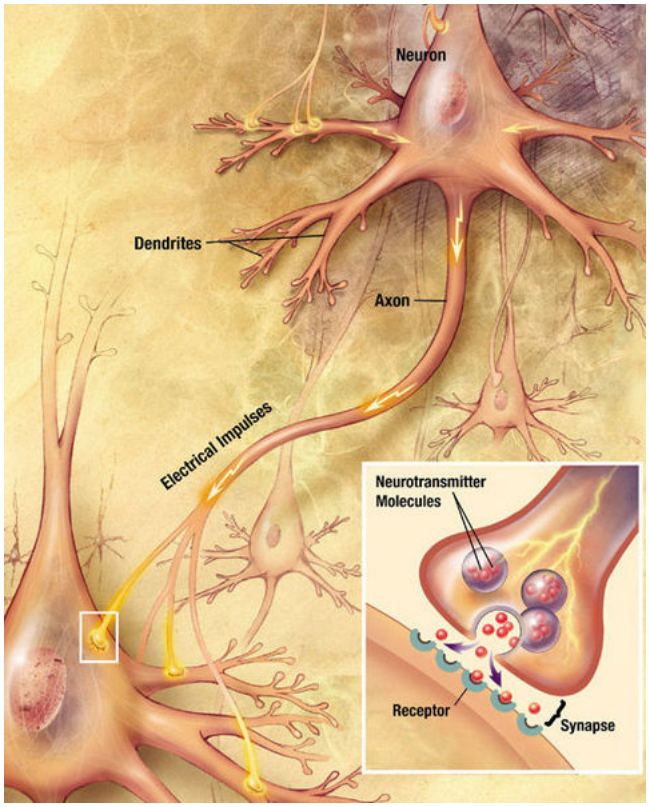

Figure 2.1 – Signal Propagation in Neurons, *Source: US National Institutes of Health, Wikimedia Commons*

The cell membrane of a resting cell is highly permeable to K^+ and only slightly permeable to Na^+. This fact in combination with the concentration gradient, generated by the Na/K pump, leads to a membrane potential of about -70 mV, i.e. the intracellular region is negatively charged with respect to the outside.

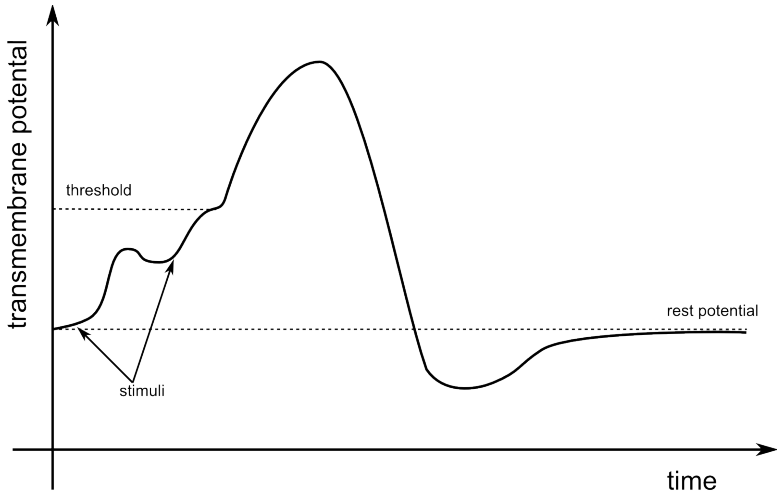

Figure 2.2 – Schematic of transmembrane potential during activation of a neuron

The energy stored in this concentration and electric gradient is used to transmit signals: When a parent neuron is activated, the synapse that connects the axon of the parent cell (presynaptic neuron) with the dendrites of the next cell (postsynaptic neuron) "fires". That means it releases neurotransmitter molecules, that increase the membrane permeability to Na^+ of the postsynaptic cell. Sodium ions now flow into the cell and the membrane potential increases (see first stimulus in Fig. 2.2) . The sodium permeability of the membrane can not only be altered by neurotransmitters, but also by the transmembrane potential itself. If the potential rises over a certain threshold, which can happen when multiple excitations arrive from parent cells, the sodium permeability increased even further. In this case an *action potential* is generated, the signal is amplified and transmitted along the axon to the synapses, which may activate following neurons.
While action potentials cause a varying electrical field, these potential changes do not show up directly in an EEG measurement. One reason is, that the amplitude of $70 - 100$ mV is very small [Moh04], and the source is additionally shielded from the electrodes by the skull, which is a weak electric conductor. Another reason is the short time range ($0.5 - 2$ ms) and the lack of synchronization of single action potentials [Plo77].
To be recorded in EEG data, neuronal activity has to be synchronous and similarly aligned. A set of neurons that fulfill these conditions are located in the so called pyramidal cells. Their dendrite trees are parallel to each other, so that on synchronous activation, a signal is generated. These activations are the main origin of the EEG data [MP95, MO06].

2.2 Mathematical Formulation

2.2.1 EEG Forward Equation

Following [HHI$^+$93] we will derive now the EEG forward equation, that describes the potential at the head surface, given a source configuration. The electromagnetic fields in the human head can be described by the quasi-static form of Maxwell's equations. This quasi-static approximation neglects temporal derivatives of the electric and magnetic field ($\frac{\partial E}{\partial t} \approx 0$ and

$\frac{\partial B}{\partial t} \approx 0$) and is only valid for fields, that do not contain high frequency components. It is well suited for bioelectric fields, where typically the highest frequency is not above 100 Hz. Together with a tissue conductivity σ of a about 0.3 S/m, the characteristic wavelength is around 65 m which is much longer than the diameter of the head.
Under these assumptions, Maxwell's equations take the following form:

$$\nabla \cdot \mathbf{E} = \frac{\rho}{\epsilon} \tag{2.1}$$

$$\nabla \cdot \mathbf{B} = 0 \tag{2.2}$$

$$\nabla \times \mathbf{E} = 0 \tag{2.3}$$

$$\nabla \times \mathbf{B} = \mu_0 \mathbf{J} \tag{2.4}$$

where $\mathbf{E}$ denotes the electric field, $\mathbf{B}$ the magnetic field, ρ the charge density, $\mathbf{J}$ the current density, ϵ the permittivity and μ_0 the permeability of free space. Since the electrical field is rotation free (2.3) we can express it as gradient of a potential ψ:

$$\mathbf{E} = \nabla \psi \tag{2.5}$$

We have seen in the section above that the bioelectric field is generated by membrane conductivity changes on the cellular level. Conductivity changes on this scale can not be resolved in a model, that consists of a whole human head. Element sizes in typical meshes are around 1 mm^3 whereas the volume of a cortical neuron is on the scale of micrometers. Therefore we assume a homogenous conductivity σ for each compartment of the head, that does not model these temporal variations on the small scale. This conductivity can also be anisotropic, in this case σ is a symmetric positive definite 3 x 3 tensor. Following [HHI$^+$93] we split the current density $\mathbf{J}$ into two components: The first part is called volume or return current $\mathbf{J}^V$. It represents the current that passively flows in reaction to the electric field, assuming the homogenous conductivity σ. Using Ohm's law in its vector form we can write the volume current as $\mathbf{J}^V = -\sigma \mathbf{E}$.
The remaining part $\mathbf{J}^P$ consists of the missing contributions, which occur due to the conductivity changes on cell scale. This current is called impressed or primary current and is the generator of the bioelectric field. So instead of modelling the conductivity changes on the cellular scale directly, we use the primary current $\mathbf{J}^P$ to model the sources.
Using this splitting, the total current density is now written as:

$$\mathbf{J} = \mathbf{J}^P + \mathbf{J}^V = \mathbf{J}^P - \sigma \mathbf{E}$$

Now we can use this expression for the source-term in Amperes law, and take the divergence of the whole equation.

$$\nabla \cdot (\nabla \times \mathbf{B}) = \mu_0 \left(\nabla \cdot \mathbf{J}^P - \nabla \cdot (\sigma \mathbf{E}) \right)$$

Using the identity $\nabla \cdot (\nabla \times \mathbf{B}) = 0$ and expressing the electric field in terms of the potential $\mathbf{E} = \nabla \psi$, we obtain:

$$\nabla \cdot (\sigma \nabla \psi) = \nabla \cdot \mathbf{J}^P \qquad \text{in } \Omega \tag{2.6}$$

where Ω denotes the open and connected head-domain.

Equation (2.6) is not a complete model, without prescribing boundary conditions on the surface of the volume conductor. We choose homogenous Neumann boundary conditions, that represent the physical fact that no currents can flow from the head to the surrounding air and vice versa.

$$(\sigma \nabla \psi) \cdot \mathbf{n} = 0 \quad \text{on } \partial\Omega \tag{2.7}$$

$\mathbf{n}$ denotes here the outward pointing normal vector on Ω.

2.2.2 Mathematical Dipole

Next we need a suitable model for the source term $\mathbf{J}^P$, so that it adequately represents an electrical activity in the brain. One assumes that the potential is generated by one or more dipoles, that can be described by a position and a dipole moment. A dipole can be seen as set of two point charges that have the same magnitude Q but different sign. They are separated by a displacement vector $\mathbf{d}$. The dipole moment of this setup is $\mathbf{p} = Q\mathbf{d}$.
The next step is to assume that the majority of the brain activity is concentrated at a single point, which is reasonable when we are dealing with EEG data recorded during a focal epileptic seizure. Therefore we need an idealization of this model where we take the limit $\mathbf{d} \to 0$. Since the dipole moment $\mathbf{p}$ should not change, the charge Q has to go to infinity [Vor11]. We have eliminated the two parameters Q and $\mathbf{d}$, by shrinking the dipole to a single position $\mathbf{x}_0$. The result of this limit is called the mathematical or current dipole, and is a widely accepted model for human brain activity [DMVDS88, HHI+93]:

$$\mathbf{J^P} = \mathbf{p} \cdot \delta(\mathbf{x} - \mathbf{x_0})$$

We will see in the section about the finite element formulation, that the strong singularity caused by the dirac delta function, needs special treatment when incorporated in the finite element method.

2.2.3 Analytical Solution

There exists an analytical solution for the EEG forward problem for the case of a multilayer sphere model, that was derived by De Munck [MP93, DM88]. In this model the head consists of concentric spheres, where every spherical shell can have different, and also anisotropic, conductivities. For practical purposes this model is not usable any more, since the error from assuming the head spherical, exceeds the errors of numerical models. However it is an important tool for validating results obtained by numerical methods.
We assume a model consisting of N concentric spheres with radii $r_N > r_{N-1} > ... > r_1$, where each space between two spheres has a constant radial and tangential conductivity, denoted as $\sigma_i^{\text{rad}} > 0$ and $\sigma_i^{\text{tang}} > 0$.
Then the potential at an electrode position $\mathbf{x}_e$, caused by a dipole at position $\mathbf{x}_0$ with dipole moment $\mathbf{p}$ is given by:

$$u_{ana}(\mathbf{x}_0, \mathbf{x}_e) = \frac{1}{4\pi} \left\langle \mathbf{p}, S_0 \frac{x_e}{r_e} + (S_1 - \cos(\omega_{0e}) S_0) \frac{x_0}{r_0} \right\rangle$$

where ω_{0e} denotes the angular distance between source and electrode and the coefficients S_0 and S_1 are defined as:

$$S_0 = \frac{F_0}{r_0}\frac{\Lambda}{(1-2\Lambda\cos(\omega_{0e})+\Lambda^2)^{3/2}} + \frac{1}{r_0}\sum_{n=1}^{\infty}\left[(2n+1)R_n(r_0,r_e) - F_0\Lambda^n\right]P_n'\cos(\omega_{0e})$$

$$S_1 = F_1\frac{\Lambda\cos(\omega_{0e})-\Lambda^2}{(1-2\Lambda\cos(\omega_{0e})+\Lambda^2)^{3/2}} + \sum_{n=1}^{\infty}\left[(2n+1)R_n'(r_0,r_e) - F_1 n\Lambda^n\right]P_n\cos(\omega_{0e})$$

P_n and P_n' denote the Legendre polynomial of n'th order and its derivative, which can be calculated using a recursion formula. For the definition of R_n, F_0, F_1 and Λ we refer to [MP93] where also a detailed derivation can be found.

2.2.4 Finite Element Formulation

We start with the EEG forward equations in their classical or strong formulation as given in (2.6) and (2.7). The main idea of the finite element method is to reformulate the problem in a so called weak version, which we will now derive.
First we have to multiply (2.6) by a function w, that is chosen from a suitable space of test functions W. Then the equation is integrated over the whole domain Ω:

$$\int_\Omega w\ \ \nabla\cdot(\sigma\nabla\psi)\,dV = \int_{\partial\Omega} w(\sigma\nabla\psi)\cdot\mathbf{n}\,dS - \int_\Omega \nabla w\cdot(\sigma\nabla\psi)\,dV$$

In this step we used Green's first identity, to shift one ∇-operator to the test function w. The boundary integral vanishes, because we assumed homogenous Neumann boundary conditions (2.7).

$$-\int_\Omega \nabla w\cdot(\sigma\nabla\psi)\,dV = \int_\Omega w(\nabla\cdot\mathbf{J}^P)\,dV \tag{2.8}$$

The treatment of the right hand side is different for each source model, and will be described in the following section.
The weak formulation of the problem now is, to find a function ψ from a suitable space U such that (2.8) is fulfilled for all $w \in W$. We can write (2.8) in a more concise way, using a bilinear functional $a : U \times W \to \mathbb{R}$ that we define as

$$a(\psi, w) := \int_\Omega \nabla w\cdot(\sigma\nabla\psi)\,dV \tag{2.9}$$

The right hand side we abbreviate by the linear functional $f : W \to \mathbb{R}$

$$f(w) := -\int_\Omega w(\nabla\cdot\mathbf{J}^p)\,dV \tag{2.10}$$

The short form of the forward problem is now:

$$\text{find } \psi \in U \ \text{ such that } \ a(\psi,w) = f(w) \ \text{ for all } w \in W \tag{2.11}$$

From now on we will set $U = W$, which is called Galerkin approach. We see that the usual

choice of $U = W = H^1(\Omega)$ causes a problem when the right hand side is modeled by a current dipole, because of the strong singularity at the dipole positions. This is the reason why we need special source models to transform the right hand side in a formulation that can be treated by the finite element method.

For a numerical solution, we use a finite dimensional function space W_h, that is a subspace of the infinite dimensional W. Assuming that W_h is spanned by the basis vectors φ_i for $i = 1..N$ we can write down a discrete version of (2.11):

$$\text{find } \psi_h \in W_h \text{ such that } a(\psi_h, w_h) = f(w_h) \text{ for all } w \in W_h$$

Since W_h is finite dimensional, the solution ψ_h can be expressed as a linear combination of its basis vectors $\psi_h = \sum_{i=1}^{N} \varphi_i \cdot u_i$.

Using the bilinearity of $a(\cdot, \cdot)$ we obtain

$$a\left(\sum_{i=1}^{N} \varphi_i \cdot u_i, \varphi_j\right) = \sum_{i=1}^{N} u_i \cdot a\left(\varphi_i, \varphi_j\right) = f(\varphi_j) \text{ for all } j = 1..N$$

The left hand side can be written as a matrix equation $A\mathbf{u} = \mathbf{f}$ with the sparse matrix A defined as

$$A = (a_{ij})_{i,j=1..N} = a(\varphi_i, \varphi_j) = \int_\Omega \nabla\varphi_j \cdot (\sigma \nabla\varphi_i)\, dV$$

The entries of the right hand side vector $\mathbf{f}$ depend on the source model used. The different source models are introduced in section 2.3.

2.2.5 Transfer Matrix

An algorithm that computes a solution to the inverse problem needs several solutions for the forward problem with changing right hand sides. When there are more right hand sides than electrode positions we can speed up the calculation by building up a so called transfer matrix [WGH04]. We use the fact that the solution is not needed on every vertex of the finite element mesh, but only on electrode positions. One introduces a restriction matrix R that maps a complete potential vector u to a vector containing only the potential at EEG electrode positions: $u_{EEG} = Ru$.

We can now express our solution vector u_{EEG} as a function of the right hand side:

$$u_{EEG} = RA^{-1}f = Tf \tag{2.12}$$

The matrix T is called transfer matrix and directly maps a right hand side to the solution vector. To obtain T we rewrite its defining formula:

$$T = RA^{-1} \;\Rightarrow\; TA = R \;\Rightarrow\; AT^T = R^T$$

In the last step we transposed both sides and exploited the symmetry of A. Now T can be obtained by solving the original system N_e times, with N_e being the number of EEG electrodes.

2.3 Dipole Models

We will now describe three existing approaches for handling the source term of the EEG forward problem.

2.3.1 Partial Integration

We begin with the first direct approach that uses *Partial Integration*, to incorporate the mathematical dipole formulation in the finite element formulation [YNH91, Vor11, LWA+09]. We rewrite the right hand side of the finite element formulation (2.8) using Green's formula (partial integration) to transfer the gradient operator from the primary current density $\mathbf{J}^P$ to the testfunction φ_i:

$$f_i = -\int_\Omega (\nabla \cdot \mathbf{J}^P)\varphi_i \, dV = \int_\Omega \mathbf{J}^P \cdot \nabla\varphi_i \, dx - \int_{\partial\Omega} \partial_{\mathbf{n}}\mathbf{J}^P \cdot \varphi_i \, dA = \int_\Omega \mathbf{J}^P \cdot \nabla\varphi_i \, dx$$

Here the integral over the boundary vanishes, using the homogenous Neumann boundary conditions (2.7). Inserting the mathematical dipole model for a dipole with moment p and position $\mathbf{x}_0$ we obtain:

$$\int_\Omega \mathbf{J}^P \cdot \nabla\varphi_i \, dx = \int_\Omega \mathbf{p} \cdot \delta(\mathbf{x} - \mathbf{x_0}) \cdot \nabla\varphi_i \, dx$$

$$f_i = \begin{cases} \mathbf{p} \cdot \nabla\varphi_i & \text{if node } i \text{ belongs to element at } \mathbf{x}_0 \\ 0 & \text{otherwise} \end{cases}$$

Note that in case of linear ansatz functions, the right hand side vector f_i does not change when the dipole is moved around in a single element, since $\nabla\varphi_i$ is constant over one element.
Strictly speaking, integration by parts requires $\mathbf{J}^P$ to be at least once continuously differentiable, which is not the case when $\mathbf{J}^P$ is modelled as a mathematical dipole that has a strong inherent singularity. Thus the partial integration has to be understood rather symbolically. To see the validity of this approach we can also start with the limit formulation of the mathematical dipole [YNH91]. A dipole consists of a source and a sink of strength I, which are separated by a small distance $\mathbf{d}$. The is equal to the mathematical dipole for $\mathbf{p} = \lim_{\mathbf{d}\to 0} I \cdot \mathbf{d}$.

$$\nabla \cdot \mathbf{J}^P = I \cdot \delta\left(\mathbf{x} - \mathbf{x_0} - \frac{\mathbf{d}}{2}\right) - I \cdot \delta\left(\mathbf{x} - \mathbf{x_0} + \frac{\mathbf{d}}{2}\right)$$

Inserting this in the right hand side of the FE weak formulation yields:

$$-\int_\Omega (\nabla \cdot \mathbf{J}^P)\varphi_i \, dV = \lim_{\mathbf{d}\to 0} I \left[\varphi_i\left(\mathbf{x}_0 + \frac{\mathbf{d}}{2}\right) - \varphi_i\left(\mathbf{x}_0 - \frac{\mathbf{d}}{2}\right)\right] = I \cdot \mathbf{d} \cdot \nabla\varphi_i(\mathbf{x}_0)$$

After substituting $\mathbf{p} = I \cdot \mathbf{d}$ we arrive at the same result as we have obtained using Green's formula.

2.3.2 Direct Approach using Venant's Principle

Another direct approach makes use of the principle of Saint-Venant, that is originated in elasticity theory. Saint-Venant's principle states, that the stresses and strains that are sufficiently

far a way from positions where the load is applied, do not depend on the exact distribution of the load but only on the static resultant of these loads. In electrostatics this corresponds to the fact that the potential due to the i'th moment of the sources decays like $\sim \frac{1}{r^{i+1}}$.
This fact is used, to substitute the original dipole source with a source field that has the same zeroth and first moment. The zeroth moment defined as $\int_\Omega \rho(\mathbf{x})\, dV$ is simply the sum or integral of all charges, which has to be zero in our case. If we additionally match the dipole moments of both distributions, the resulting error in the potential, due to redistribution of the sources, decays like $\sim \frac{1}{r^3}$. By taking higher order moments into account one can further decrease the error made by the substitution of the source field.
We follow the ideas of [BKF+97, WABH07, Vor11] to substitute the mathematical dipole by a set of point sources on nearby finite element nodes. If we want to model a dipole at position x_0, we first look for the finite element node x_1, that is closest to this position. To ensure a spatial locality of the resulting load distribution we choose to only apply loads on the neighboring nodes of x_1 which we name $x_2, x_3, ..., x_k$. In a cubic mesh every node has 27 neighbors, whereas in a tetrahedral mesh the number of neighbors is around 30. The node x_1 itself, does not receive any loads since the dipole position x_0 may get arbitrary close to this node, resulting in a very high load on x_1 that could lead to numerical instabilities [Vor11].
The moments of this source distribution can be written as function of the loads q_i:

$$ {}^lT = \sum_{i=2}^{k} (x_i - x_0)^l q_i = \sum_{i=2}^{k} \Delta x_i^l q_i \tag{2.13} $$

To ensure a decay of this series we normalize the distances Δx_i by a proper reference length a^{ref} [BKF+97] that has to fulfill the following relation:

$$ (\Delta\overline{x_i})_j = \left(\frac{(\Delta x_i)_j}{a^{ref}} \right) \overset{!}{<} 1 $$

The index j stands here for the cartesian dimensions $\{x, y, z\}$.
Equation (2.13) can be written in matrix form using the the normalized moments and distances:

$$ \overline{t}_j := \begin{pmatrix} ({}^0\overline{T})_j \\ ({}^1\overline{T})_j \\ \vdots \\ ({}^n\overline{T})_j \end{pmatrix} = \begin{pmatrix} (\Delta\overline{x}_1)_j^0 & (\Delta\overline{x}_2)_j^0 & \dots & (\Delta\overline{x}_k)_j^0 \\ (\Delta\overline{x}_1)_j^1 & (\Delta\overline{x}_2)_j^1 & \dots & (\Delta\overline{x}_k)_j^1 \\ \vdots & \vdots & \ddots & \vdots \\ (\Delta\overline{x}_1)_j^n & (\Delta\overline{x}_2)_j^n & \dots & (\Delta\overline{x}_k)_j^n \end{pmatrix} \cdot \begin{pmatrix} q_1 \\ q_2 \\ \vdots \\ q_n \end{pmatrix} =: \overline{X}_j \cdot q \tag{2.14} $$

In case of a point dipole, the moments $({}^0\overline{T})_j$ are zero for $l > 2$. For $l = 0..2$ they are given by:

$$ {}^l\overline{T} = \frac{1 - (-1)^l}{(2a^{ref})^l} \cdot p \tag{2.15} $$

Our goal is to solve equation (2.14) for the vector q.
Since this equation system is underdetermined, we add a regularizer, using the Tikhonov matrix $\overline{W}_j = \mathrm{diag}((\Delta\overline{x}_1)_j, (\Delta\overline{x}_2)_j, ..., (\Delta\overline{x}_k)_j))$. The vector q can then be calculated as a minimum of the following functional:

$$ F_\lambda(q) = ||\overline{t}_j - \overline{X}_j q||_2^2 + \lambda ||\overline{W}_j q||_2^2 \tag{2.16} $$

The Tikhonov regularizer $||\overline{W}_j q||_2^2$ favors loads with small absolute value, that are located near x_0. Thus it leads to a high spatial concentration of loads at this point, that are chosen as small as possible. To get an expression for the q we first differentiate with respect to q_i and get:

$$(\overline{X}_j^T \overline{X}_j + \lambda \overline{W}_j^T \overline{W}_j) q = \overline{X}_j^T \overline{t}_j \tag{2.17}$$

Solving for q gives as the resulting load distribution:

$$q = \left[\sum_{j=1}^{3} (\overline{X}_j^T \overline{X}_j + \lambda \cdot \overline{W}_j^T \overline{W}_j) \right]^{-1} \cdot \sum_{j=1}^{3} \overline{X}_j^T \overline{t}_j$$

For the computations with the SimBio toolkit the following parameter values were used [Vor11]: $a^{ref} = 20\text{mm}$, $n = 2$, and $\lambda = 10^{-6}$.
We now come to the assembly of the right hand side vector $\mathbf{f}$, used in the finite element computation. Following [BKF+97, WAT+06] we now express the divergence of the primary current $\mathbf{J}^P$ using the source vector q:

$$\nabla \cdot \mathbf{J}^P = \sum_{i=2}^{k} q_i \delta(\mathbf{x} - \mathbf{x_l})$$

Using this representation together with (2.10) yields:

$$f_j = f(\varphi_j) = -\int_\Omega \varphi_j \, \nabla \cdot \mathbf{J}_P \, dV = -\int_\Omega \varphi_j \sum_{i=2}^{k} q_i \delta(\mathbf{x} - \mathbf{x_l}) \, dV = -\sum_{i=2}^{k} q_i \int_\Omega \varphi_j \delta(\mathbf{x} - \mathbf{x_l}) \, dV$$

The term $\delta(\mathbf{x} - \mathbf{x_l})$ can only be one or zero, since the positions $\mathbf{x}_l$ are located at grid nodes, where the hat function φ_j is either one or vanishes.

$$f_j = \begin{cases} -q_l & \text{if } j\text{'th vertex is at position } \mathbf{x}_l \\ 0 & \text{otherwise} \end{cases}$$

2.3.3 Full Subtraction Approach

Following [LWA+09, DWD+09] we present another source model for the EEG forward problem, called the subtraction approach. In contrast to the already described source models, the subtraction approach handles the source singularity, caused by the current dipole, indirectly. This is done by splitting up the potential ψ into two parts:

$$\psi = \psi_0 + \psi_{corr}$$
$$\sigma = \sigma_0 + \sigma_{corr}$$

ψ_0 is defined as the solution of a current dipole in an unbounded homogenous medium with constant conductivity σ_0.

$$\nabla \cdot (\sigma_0 \nabla \psi_0) = \nabla \cdot \mathbf{J}^P = \nabla \cdot (\mathbf{p}\, \delta(\mathbf{x} - \mathbf{x}_0)) \tag{2.18}$$

The conductivity σ_0 is assumed to be constant in a nonempty subdomain Ω_0 around then source position $\mathbf{x}_0$ (*homogeneity condition*), while the remaining part σ_{corr} is zero in Ω_0.
Using these definitions, we can write down an analytical solution for (2.18), and later use the decomposition to remove the singularity at the right hand side.
We first handle the case of an isotropic conductivity. In this case σ is a scalar and the analytical solution for a dipole at position $\mathbf{x_0}$ and moment $\mathbf{p}$ is given by:

$$\psi_0(\mathbf{x}) = \frac{1}{4\pi\sigma_0} \frac{\mathbf{p} \cdot (\mathbf{x} - \mathbf{x_0})}{||\mathbf{x} - \mathbf{x_0}||_2}$$

In the anisotropic case σ_0 is a symmetric positive definite 3×3 tensor, and the analytical solution is:

$$u_0(x) = \frac{1}{4\pi\sqrt{\sigma_0}} \frac{\mathbf{p} \cdot \sigma_0^{-1}(\mathbf{x} - \mathbf{x_0})}{\left((\mathbf{x} - \mathbf{x_0})^T \sigma_0^{-1}(\mathbf{x} - \mathbf{x_0})\right)^{3/2}}$$

Now we subtract the solution for ψ_0 (2.18) from (2.6) and obtain:

$$\nabla \cdot (\sigma \nabla \psi_{corr}) = -\nabla \cdot (\sigma_{corr} \nabla \psi_0) \tag{2.19}$$

$$\sigma \partial_{\mathbf{n}} \psi_{corr} = -\sigma \partial_{\mathbf{n}} \psi_0 \tag{2.20}$$

This formulation can be used to numerically calculate a solution for ψ_{corr} since ψ_0 is known. Therefore we rewrite (2.19) and (2.20) to obtain a weak formulation using a testfunction φ_i. The right hand side vector $\mathbf{f}$ is then given as:

$$f_i = -\int_\Omega \sigma_{corr} \nabla \psi_0 \cdot \nabla \varphi_i \, dV - \int_{\partial\Omega} \sigma_0 \partial_{\mathbf{n}} \psi_0 \cdot \varphi_i \, dS$$

The bilinear form $a(\cdot, \cdot)$ and the stiffness matrix A stay the same, however instead of computing the solution $\mathbf{u}$ directly, we only compute $\mathbf{u}_{corr}$ numerically. Then the analytical part $\mathbf{u}_0$ is added, to arrive at the solution $\mathbf{u}$.
Note that the right hand side vector $\mathbf{f}$ is not sparse, as it is for the other dipole models. This leads to a higher computational demand and an increased runtime, as we will see in Section 5.4.

3 Differential Geometry and Whitney Forms

In the following chapter we will give an introduction to differential geometry, the mathematical discipline, which provides the theory of Whitney forms, which can be used in the finite element method as Whitney elements. We first define important concepts, like differential forms and exterior derivative in a continuous setting, and then describe how these can be transferred to the discrete world.

3.1 Continuous Differential Geometry

3.1.1 Manifolds

The natural setting of differential geometry are *manifolds*. Manifolds are topological spaces which are locally homeomorphic to $\mathbb{R}^n$. This means, that for every point in the manifold M, there has to exist a neighborhood that is topologically the same as an open ball in $\mathbb{R}^n$. To develop an intuitive understanding one can imagine a manifold as a subset of euclidean space, for example a sphere, a cylinder or a torus. Consider the surface of a sphere, which is curved on a global scale, but any small region around a point can be flattened to a circular region on a plane. To describe a manifold mathematically one introduces the concept of charts. A chart is a function which maps a specific region of the manifold to euclidean space. A collection of charts that cover the whole manifold and are consistent in the region where they overlap, are called an atlas for the manifold. Polar coordinates are an example for a possible chart of the sphere. However there are more charts needed, because of the singularity of polar coordinates at the poles.

Because a manifold is locally Euclidean we can define for each point q the so called *tangent space* TM_q, which consists of all tangent vectors to M at q. Note that there are different tangent spaces at each point of the manifold. The union of all theses spaces are termed *tangent bundle*. This generalizes the notion of a "bound vector" in Euclidean space. The tangent spaces are needed to define vector fields on manifolds. The vectors themselves are not elements of the manifold but lie in the tangent space of their associated point. Tangent vectors are *contravariant* tensors and are denoted with upper indices $\mathbf{v}^i$.

Any vector space has a dual space consisting of all linear functionals, that map elements of the original vector space to the real numbers. The dual space of the tangent space is called cotangent space T^*M_q and its elements are the functions $\tilde{\mathbf{v}} : TM_q \to \mathbb{R}$. We can find a basis $\tilde{\sigma}^i$ of the dual space using a basis of the tangent space $\mathbf{e}^j$ by the following condition:

$$\tilde{\sigma}_i(\mathbf{e}^j) = \delta_i^j$$

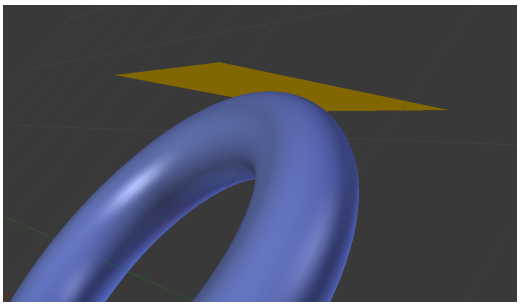

Figure 3.1 – Tangential Space on a Torus

We pick these functionals as a basis which evaluate to 1 on a specific unit vector and to 0 on all other basis vectors.

3.1.2 Differential 1-forms

Lets begin our investigation of differential forms and integration with single variable calculus. In one dimension there already exist different notions of an integral [Tao07]. First there is the concept of the *indefinite integral* or anti-derivative $\int f(x)\ dx$ that is basically the reverse of differentiation. A very similar notion in one dimension, is the *definite* integral $\int_a^b f(x)\ dx$ which is related to the indefinite integral by

$$\int_a^b f(x)\ dx = F(b) - F(a) \quad \text{where} \quad F(x) = \int f(x)\ dx$$

When one goes to higher dimensions, the differences between these two concepts become more evident. The indefinite integral generalizes to *solutions of differential equations* [Tao07], which we will not pursue any further. More interesting for our purposes is the generalization of the definite integral to differential forms.
A one dimensional integral is approximated by the sum

$$\int_a^b f(x)\ dx \approx \sum_{i=0}^{n=1} f(x_i)(x_{i+1} - x_i) \tag{3.1}$$

where the x_i form a discrete path going from a to b : $x_0 = a, x_1, ..., x_n = b$. Here the choice of the path does not influence the value of the integral, we could even go some steps backward and cover some interval twice. As long as we assume that the stepsize of the path $\sup |x_{i+1} - x_i|$ goes to zero, the forward and reverse steps will cancel each other out.
Now lets do the generalizations to an n-dimensional manifold. The interval $[a, b]$ is replaced by the parametrized curve $\gamma : [0, 1] \to M^n$. The equivalent of the increment $x_{i+1} - x_i$ is the tangent vector $\mathbf{v_T}$ on the curve γ, which is an element of the tangent space TM. In the one dimensional case the integral was approximated by summing up increments, that where scaled by the value of the function at this point (3.1). In higher dimensions this scaling operation generalizes to a linear functional of the increment, i.e. a functional of the tangent vector.

We rewrite (3.1) with the integrand as a linear function:

$$\int_\gamma df = \sum_{i=0}^{n=1} df(\Delta \mathbf{x}) \tag{3.2}$$

Our new object df, which we call differential 1-form, is a linear mapping from the tangent space to the real numbers. This means that differential forms are nothing more than elements of the cotangent space of a manifold. The linear mapping is specified by the function that has to be integrated:

$$df = TM_q \to \mathbb{R}: \quad df(\mathbf{v}) = \sum_j \frac{\partial f}{\partial x_j} v_j \tag{3.3}$$

3.1.3 p-vectors and p-forms

So far we have introduced differential 1-forms as objects that can be integrated over one variable. We have formally defined them as elements of the cotangent space of a manifold. Now we want to follow the same path for arbitrary n-forms, i.e. objects like $f(x, y)dx\,dy$ that can be integrated over multiple variables.
Therefore we need concepts from multilinear algebra: the exterior product and multivectors. The exterior- or wedge product is a bilinear, anticommutative form defined on an vector space:

$$(a\mathbf{x} + b\mathbf{y}) \wedge \mathbf{z} = a(\mathbf{x} \wedge \mathbf{z}) + b(\mathbf{y} + \mathbf{z})$$

$$\mathbf{x} \wedge \mathbf{y} = -\mathbf{y} \wedge \mathbf{x}$$

From the anticommutativity directly follows that $\mathbf{x} \wedge \mathbf{x} = 0$. The wedge product can be used to create multivectors. Objects like $\mathbf{x} \wedge \mathbf{y}$ are called 2-vectors and form the basis of another vector space $\bigwedge^2 V$. A 2-vector can be viewed as an object consisting of two 1-vectors, since there are two directions encoded in it. The magnitude of the 2-vector is the area of the parallelogram spanned by the 1-vectors. To see this, we calculate the wedge product of two vectors in $\mathbb{R}^2$.

$$(a\mathbf{e_1} + b\mathbf{e_2}) \wedge (c\mathbf{e_1} + d\mathbf{e_2}) =$$

$$= ac(\mathbf{e_1} \wedge \mathbf{e_1}) + bd(\mathbf{e_2} \wedge \mathbf{e_2}) + ad(\mathbf{e_1} \wedge \mathbf{e_2}) + bc(\mathbf{e_2} \wedge \mathbf{e_1}) =$$

$$= (ad - bc)(\mathbf{e_1} \wedge \mathbf{e_2}) = \begin{vmatrix} a & c \\ b & d \end{vmatrix} (\mathbf{e_1} \wedge \mathbf{e_2})$$

Now lets have a close look on the new vector space of two vectors $\bigwedge^2 V$, called the product space. The basis vectors of a product space $\bigwedge^p V$ are products of basis vectors of V, as one can see in the following example.
Let $V = \mathbb{R}^3$ with basis vectors $\{\mathbf{e}_1, \mathbf{e}_2, \mathbf{e}_3\}$.
The standard basis of $\bigwedge^2 \mathbb{R}^3$ is $\{\mathbf{e}_1 \wedge \mathbf{e}_2, \mathbf{e}_2 \wedge \mathbf{e}_3, \mathbf{e}_1 \wedge \mathbf{e}_3\}$. Other possible combinations of the basis vectors are either zero, when both basis vectors are equal, or are the negative of already listed basis vectors (anticommutativity).
The dimension of the product space $\bigwedge^n V$ of an n dimensional vector space V is $\binom{n}{p}$. To construct a basis vector for the product space one has to choose p distinct basis vectors out

of the basis set which has size n. The order of the chosen basis vectors of V does not matter, because permuting the indices only changes the sign of the outcome.

3.1.4 Exterior Derivative

Our goal is to give a formal definition of integrands as differential forms. For integrands that involve the integration over one variable we have already achieved that by defining differential 1-forms as elements of the cotangent space of a manifold. Having the multivector concept available, we can now define integrands over n variables as elements of $\bigwedge^n T^*M_q$. An integrand over two variables is then written as $f(x,y)\, dx \wedge dy$. The operation that maps k forms to $k+1$ forms is called exterior derivative $\left(d : \bigwedge^k T^*M \to \bigwedge^{k+1} T^*M\right)$.

Let $\tilde{\alpha}$ be a p form and $\tilde{\beta}$ be a q form then:

$$d(\tilde{\alpha} + \tilde{\beta}) = d\tilde{\alpha} + d\tilde{\beta} \qquad \text{Linearity} \tag{3.4}$$

$$d(\tilde{\alpha} \wedge \tilde{\beta}) = d\tilde{\alpha} \wedge \tilde{\beta} + (-1)^p \tilde{\alpha} \wedge d\tilde{\beta} \qquad \text{Product Rule} \tag{3.5}$$

$$d(d\tilde{\alpha}) = 0 \qquad d \text{ is nilpotent} \tag{3.6}$$

Note that we have already defined the exterior derivative of a real valued function, or a 0-form, as the ordinary differential of the function (3.3).
To show the power of this new formalism, we demonstrate how one can calculate the differential surface element in polar coordinates $dr \wedge d\phi$ starting from Cartesian coordinates $dx \wedge dy$.

$$\begin{aligned} dx \wedge dy &= d(r\cos(\phi)) \wedge d(r\sin(\phi) = \\ &= (dr\cos\phi + r \cdot d(\cos\phi)) \wedge (dr\sin\phi + r d(\sin\phi)) = \\ &= r\cos^2\phi(dr \wedge d\phi) - r\sin^2(d\phi \wedge dr) = \\ &= r(dr \wedge d\phi) \end{aligned}$$

Here again we see the strong relation of the wedge product with determinants. What we have done above, is basically computing the functional determinant of the coordinate transformation.

The common differential operators from standard vector calculus can be expressed in a coordinate invariant formulation, using the formalism of exterior derivatives and differential forms. We start by demonstrating that for the *curl* operator. Since the exterior derivative is only defined on forms, we have to express our vector field as a differential form. The field $\omega = (A, B, C)^T$ becomes $\tilde{\omega}^1 = A \wedge dx + B \wedge dy + C \wedge dz$. Here the superscript on the differential form tells us how the vector field was converted to a differential form. We will see that there are other ways to convert a vector field to a differential form.
Lets now calculate the exterior derivative of this field:

$$d\tilde{\omega} = dA \wedge dx + dB \wedge dy + dC \wedge dz + Ad(dx) + Bd(dy) + Cd(dz) =$$

$$
\begin{aligned}
&= \frac{\partial A}{\partial x}dx + \frac{\partial A}{\partial y}dy + \frac{\partial A}{\partial z}dz + \\
&+ \frac{\partial B}{\partial x}dx + \frac{\partial B}{\partial y}dy + \frac{\partial B}{\partial z}dz + \\
&+ \frac{\partial C}{\partial x}dx + \frac{\partial C}{\partial y}dy + \frac{\partial C}{\partial z}dz \\
= \left(\frac{\partial C}{\partial y} - \frac{\partial B}{\partial z}dy \wedge dz\right) &+ \left(\frac{\partial A}{\partial z} - \frac{\partial C}{\partial x}dz \wedge dx\right) + \left(\frac{\partial B}{\partial x} - \frac{\partial A}{\partial y}dx \wedge dy\right)
\end{aligned}
$$

The components of the new vector field indeed match the ones obtained when calculating $\nabla \times \omega$, however this resulting vector field now lies in a different space $\bigwedge^2 T^*M$. This is not surprising, since we calculated an exterior derivative and thus increased the order of the differential form by one degree. But our new space is also a 3-dimensional vector space, thus there exists an isomorphism between these spaces.
In general the spaces $\bigwedge^p V$ and $\bigwedge^{(n-p)} V$ have the same dimension due to the symmetry of the binomial coefficient $\binom{n}{p} = \binom{n}{(n-p)}$. The so called *hodge star operator* is an isomorphism between these spaces. It is denoted as $*$ and is formally defined as:

$$*(\mathbf{e}_{i_1} \wedge \mathbf{e}_{i_2} \wedge ... \wedge \mathbf{e}_{i_k}) = \mathbf{e}_{i_{k+1}} \wedge \mathbf{e}_{i_{k+2}} ... \wedge \mathbf{e}_{i_n}$$

where $(i_1, i_2, ..., i_k, i_{k+1}, ..., i_n)$ is an even permutation.
For $V = \mathbb{R}^3$ this means:

$$
\begin{aligned}
*(\mathbf{e}_1 \wedge \mathbf{e}_2) &= \mathbf{e}_3 \\
*(\mathbf{e}_2 \wedge \mathbf{e}_3) &= \mathbf{e}_1 \\
*(\mathbf{e}_3 \wedge \mathbf{e}_1) &= \mathbf{e}_2
\end{aligned}
$$

Using the Hodge star and the exterior derivative we can now express the *curl* of a vector field ω :

$$\text{curl}(\omega) = *(d\tilde{\omega}^1) \tag{3.7}$$

To calculate the *curl* we have expressed the vector field as a 1-form. We could also have expressed it as a 2-form because $\bigwedge^2 T^*M$ is also 3-dimensional. The way we express our vector field is crucial for the outcome of the calculation. Lets see what happens when we compute the exterior derivative of a vector field expressed as a 2 form:

$$
\begin{aligned}
d\tilde{\omega}^2 = d\left(A \wedge dy \wedge dz + B \wedge dz \wedge dx + C \wedge dx \wedge dy\right) &= \\
= \left(\frac{\partial A}{\partial x}dx + \frac{\partial A}{\partial y}dy + \frac{\partial A}{\partial z}\right) \wedge dy \wedge dz &+ \\
+ \left(\frac{\partial B}{\partial x}dx + \frac{\partial B}{\partial y}dy + \frac{\partial B}{\partial z}\right) \wedge dz \wedge dx &+ \\
+ \left(\frac{\partial C}{\partial x}dx + \frac{\partial C}{\partial y}dy + \frac{\partial C}{\partial z}\right) \wedge dx \wedge dy &= \\
= \left(\frac{\partial A}{\partial x}dx + \frac{\partial B}{\partial y}dy + \frac{\partial C}{\partial z}\right) \wedge dx \wedge dy \wedge dz &
\end{aligned}
$$

If we now take the Hodge star of the result we obtain the divergence because $*(dx \wedge dy \wedge dz) = 1$.

$$\mathrm{div}(\omega) = *(d\tilde{\omega}^2) = *d * \tilde{\omega}^1 \tag{3.8}$$

When we express the *curl* and *grad* operator in the language of differential forms, we see that the vector equations $\nabla \times (\nabla f) = 0$ and $\nabla \cdot (\nabla \times f) = 0$ are only special cases of the equation $d(d\omega) = 0$.

3.1.5 Generalized Stokes' Theorem

In the framework of differential geometry Gauss's divergence theorem and Stokes' theorem are special cases of the *Generalized Stokes' Theorem* :

$$\int_{\Omega} d\tilde{\omega} = \int_{\partial\Omega} \tilde{\omega} \tag{3.9}$$

where Ω denotes a p-dimensional manifold with boundary $\partial\Omega$ and $\tilde{\omega}$ is a differential $(p-1)$ form.
Integration can be seen as a bilinear pairing of the domain and the integrand. It is is linear in the integrand: $\int_\Omega \sum_i f_i(x)\, d\omega = \sum_i \int_\Omega f_i(x)\, d\omega$ and linear in the domain, when we assume that the Ω_i's are disjoint, and the addition of two domains is defined as their union: $\int_{\sum_i \Omega_i} \sum_i f_i(x)\, d\omega = \sum_i \int_{\Omega_i} f_i(x)\, d\omega$.
If we write the above theorem in a slightly different form, that emphasizes the bilinear nature, we see that the exterior derivative is the adjoint operation to the boundary operator.

$$\langle d\tilde{\omega}, \Omega \rangle = \langle \tilde{\omega}, \partial\Omega \rangle$$

The exterior derivative is strongly connected to topology. It is a basic topological fact, that the boundary of a manifold, that is itself a boundary of a higher dimensional manifold, is always empty ($\partial\partial\Omega = 0$) . From this statement follows that the exterior derivative of an exterior derivative has to be zero ($d(d\omega) = 0$):

$$0 = \int_{\partial(\partial\Omega)} \omega = \int_{\Omega} d(d\omega)$$

3.2 Discrete Differential Forms

3.2.1 Cell Complex

In the last section we gave a brief overview of the field of differential geometry. We now continue with discrete differential geometry, which provides discrete analogues of the concepts we have seen previously.
Lets begin with the notion of a *cell complex*. A cell basically is a component of a mesh. Consider a triangular mesh in three dimensional space, then a 0-cell is a vertex, a 1-cell an edge, a 2-cell a triangle and a 3-cell is a tetrahedron (see Figure 3.2) . The strict mathematical definition of cells uses the concept of homeomorphism: A p-cell is defined as a set of points that is homeomorphic to a closed unit p-ball [BS08], i.e. there exists a continuous function

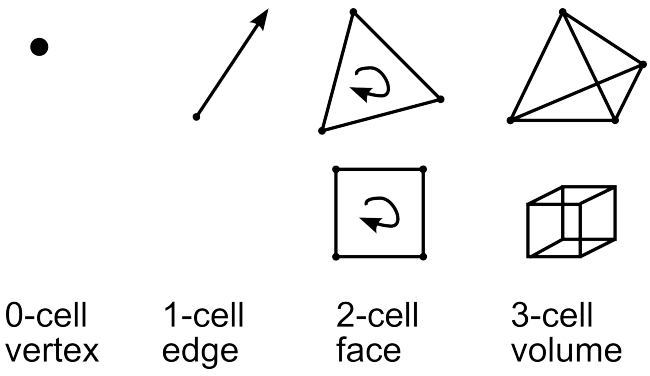

Figure 3.2 – Examples of cells

between the cell and the unit ball that maps the ball onto the cell and vice versa. Note that this definition does not require the cells to be simplices.

For a collection of p-cells to form a valid mesh or *cell complex*, certain conditions have to be fulfilled [DKT08]:

1. The intersection of two p-cells is either empty or on the boundary of both cells

2. The boundary of a p-cells entirely consists of a collection of $(p-1)$ cells

3.2.2 Orientation

Until now, a cell complex contains information about the positions of the cells and how they are connected. In order to do integral calculations on that mesh, we also need an orientation of the cells. When we want to calculate the flux of a vector field through a surface, we need a normal vector to that surface. There are two choices for that normal vector which determines the sign of the integration result. In the continuous setting we have to orient surfaces, before integrating over them, and the same is true in the discrete setting.

For every p-cell we can define an orientation by ordering the vertices of that cell. For an edge, consisting of the vertices v_1 and v_2, we can specify two directions/orientations: (v_1, v_2) and (v_2, v_1). A face can also be oriented in two ways: clockwise and counterclockwise. These orientations are usually described by a vertex ordering, for example (v_1, v_2, v_3). By interchanging two vertices in this ordering, we change the orientation of the face. Generally the orientation can take on the values ± 1 and is defined by the signum of the vertex permutation. From now on we assume that we have given a prescribed ordering for each cell in the cell complex.

Each p-cell induces an orientation on its boundary $(p-1)$-cells that may or may not be the same as the prescribed orientation. Consider the face with given orientation (v_3, v_2, v_1) in Figure 3.3. The induced orientation matches the orientation of e_3 and contradicts the orientation of e_1 and e_2. The face can be seen as a signed sum of its boundary. In this example the face can be expressed as $f_1 = -e_1 - e_2 + e_3$.

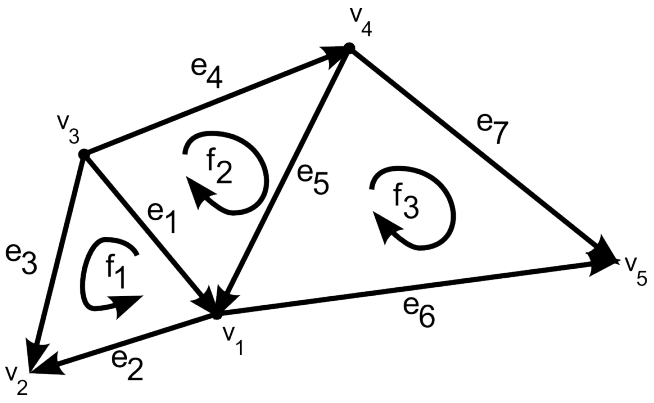

Figure 3.3 – Induced Orientation and Incidence Matrix

3.2.3 Incidence Matrix

A well known construct from graph theory is the incidence matrix. It describes how vertices are connected, to form edges, or which edges form a face together. In the language of discrete differential calculus the incidence matrix I_p describes the relationship between $(p-1)$- and p-cells. Each row of the matrix describes a p-cell as a signed sum of its boundary. There is a row for each p-cell so that this data-structure describes the relationship between all p and $(p-1)$ cells.

$$I_p(a,b) = \begin{cases} +1, & \text{if } b \text{ is on boundary of } a, \text{ orientations match} \\ -1, & \text{if } b \text{ is on boundary of } a, \text{ orientations don't match} \\ 0, & \text{if } b \text{ is not on boundary of } a \end{cases}$$

Lets do an example and write down the incidence matrix of the graph depicted in Figure 3.3. The matrix has two rows, one for each face, and 5 columns for the edges:

$$I_2 = \begin{pmatrix} -1 & -1 & 1 & 0 & 0 & 0 & 0 \\ -1 & 0 & 0 & 1 & 1 & 0 & 0 \\ 0 & 0 & 0 & 0 & -1 & -1 & 1 \end{pmatrix}$$

3.2.4 Chains

In the discrete setting, domains of integration are specified by choosing a set of p-cells, together with an orientation for these cells. This can be done using an *indicator vector* that contains the values 0, -1 and $+1$. Zero means, that cell is not part of the domain, the values ± 1 include the cell into the domain and specify the orientation. Such an indicator vector which assigns a scalar to each p-cell is called a p-chain. p-chains are the analogues to p-vectors in the continuous theory.

3.2.5 Boundary Operator

Now we can use chains and the incidence matrix to get a discrete version of the boundary operator "∂". When we multiply a domain (which is represented by a p-chain) from the right

to the incidence matrix we get a $(p-1)$-chain that represents the boundary. We will demonstrate this on the example cell complex from Figure 3.3. Let our domain consist out of the first two faces in clockwise direction. That means our domain is the 2-chain $\tau = (-1, 1, 0)^T$. When we apply the boundary operator on this chain we get a 1-chain that has nonzero values on the boundary edges.

$$\partial\tau = I_2^T\tau = \begin{pmatrix} -1 & -1 & 1 & 0 & 0 & 0 & 0 \\ -1 & 0 & 0 & 1 & 1 & 0 & 0 \\ 0 & 0 & 0 & 0 & -1 & -1 & 1 \end{pmatrix}^T \cdot \begin{pmatrix} -1 \\ 1 \\ 0 \end{pmatrix} = \begin{pmatrix} 0 & 1 & -1 & 1 & 1 & 0 & 0 \end{pmatrix}^T$$

We have now seen two aspects of the incidence matrix: it encodes the topology of the cell complex and is also a representation of the discrete boundary operator.

3.2.6 Cochains

Having seen the discrete versions of domains and the boundary operator we now move on to the key concept: discrete differential forms. Continuous differential forms are the duals of tangent (multi-) vectors i.e. they are linear maps from the tangent space to the real numbers. We have seen that tangent vectors correspond to p-chains. So we are looking for the dual of a p-chain τ.

$$\tilde{\omega} : \tau \to \mathbb{R}$$

This object $\tilde{\omega}$ is called cochain. A cochain can also be represented by a vector with one value per cell, since the chains form a vector space, and one only needs to know the values of the linear mapping for each basis vector of the original space, to have the linear mapping fully specified. Thus an evaluation of a cochain on a chain $\tilde{\omega}(\tau)$ can be done by calculating the inner product of their two vector representations $\tilde{\omega}^T\tau$.
The evaluation of a cochain on a chain corresponds to integrating a differential form on a domain. A p dimensional domain is given by the p-chain $\sum_i c_i\sigma_i$ where σ_i are the p-cells of a cell complex. Now we integrate a form/cochain ω on this domain [DKT08].

$$\int_{\sum_i c_i\sigma_i} \tilde{\omega} = \sum_i c_i \cdot \left(\int_{\sigma_i} \tilde{\omega} \right) = \sum_i c_i\tilde{\omega}_i$$

The second term is the inner product we have used, to apply a cochain to a chain. The integrals $\int_{\sigma_i} \omega$ are therefore the components of the cochain vector.

3.2.7 Interpolation with Whitney Forms

We have argued in the last section, that cochains are the discrete analogon to differential forms. They are represented as vectors where the components correspond to the value of the differential form on a cell. Assuming we have given a 2-cochain, then its vector representation has a component for each face that tells us the flux across this face.
We will see that in our application it is not enough to know the value of a p-cochain on each p-cell, we also have to be able to obtain pointwise values of it. Therefore we need an interpolation of these cochains to the rest of the space.
For 0-cochains (i.e. vectors with entries for each vertex) this is well known from the finite element method. We introduce so called *hat functions* φ_i, with the defining property that they

have unit value on one vertex of the mesh and zero value on all others. In between they are piecewise linear:

$$\varphi_i = 1 \text{ on } v_i \qquad\qquad \varphi_i = 0 \text{ on } v_j \text{ for } i \neq j$$

The value of a 0-cochain $\tilde{\omega}$ at a point $\mathbf{p}$ can then be obtained by $\tilde{\omega}(\mathbf{p}) = \sum_i \tilde{\omega}_i \varphi_i(\mathbf{p})$.

The generalization of this concept to p-cochains was done by Whitney [Whi57]. The formulation for the general Whitney p-form on a cell σ with vertices $i_0, i_1, .., i_k$ reads [DKT08]:

$$\varphi_{\sigma_{i_0,i_1,\ldots,i_k}} = k! \sum_{j=0}^{k} (-1)^j \varphi_{i_j} d\varphi_{i_0} \wedge \cdots \wedge \widehat{d\varphi_{i_j}} \cdots \wedge d\varphi_{i_k} \tag{3.10}$$

where the hat over φ_{i_j} means, that this factor has to be left out.

Lets first do the special case for Whitney 1-forms to get familiar with this definition. A Whitney 1-form is associated with an edge σ_{ij}, that connects v_i with v_j. It can be written using the hat functions of its vertices in the following way:

$$\varphi_{\sigma_{ij}} = \varphi_i \, d\varphi_j - \varphi_j \, d\varphi_i$$

When the Whitney form is integrated over its associated edge it evaluates to ± 1 (depending on the orientation), integration over other edges is zero:

$$\int_{\sigma_{ab}} \varphi_{\sigma_{ij}} = \begin{cases} 1 & \text{for } a = i \text{ and } b = j \\ -1 & \text{for } a = j \text{ and } b = j \\ 0 & \text{otherwise} \end{cases}$$

For the application in the EEG forward problem we will need Whitney 2-forms. Using the general definition (3.10) for $k = 2$ we get:

$$\mathbf{w}_{ijk} = \varphi_{\sigma_{ijk}} = 2! \, (\varphi_i \, d\varphi_j \wedge d\varphi_k + \varphi_j \, d\varphi_k \wedge d\varphi_i + \varphi_k \, d\varphi_i \wedge d\varphi_j)$$

Note the new notation for Whitney functions of degree 2 consisting of vertices i,j,k as $\mathbf{w}_{ijk}$. Again the integral over the associated face σ_{ijk} has to be one, whereas the integral over all other faces has to be zero. To see that the integral over a different face σ_{abc} yields zero, note that there is at least one vertex that does not belong to the face σ_{ijk}, so its hat function has zero value everywhere on σ_{abc}. Since the hat function occurs in every term, the complete integral is zero.

To see that the integral over the associated face itself yields one, we have to do the integration explicitly:

$$\int_{\sigma_{ijk}} \mathbf{w}_{ijk} = 2 \int_{\varphi_i=0}^{1} \int_{\varphi_j=0}^{1-\varphi_i} \varphi_i \, (d\varphi_j \wedge d(1-\varphi_i-\varphi_j)) + \varphi_j \, (d(1-\varphi_i-\varphi_j)) \wedge d\varphi_i + (1-\varphi_i-\varphi_j)) \, \varphi_i \wedge \varphi_j =$$

Here we used the fact that the hat functions form a partition of unity on σ_{ijk}.

$$2\int_{\varphi_i=0}^{1}\int_{\varphi_j=0}^{1-\varphi_i} -\varphi_i(d\varphi_j\wedge d\varphi_i)-\varphi_j(d\varphi_j\wedge d\varphi_i)+(d\varphi_i\wedge d\varphi_j)-\varphi_i(d\varphi_i\wedge d\varphi_j)-\varphi_j(d\varphi_i\wedge d\varphi_j)=$$

Using the properties of the exterior derivative (3.6) we get:

$$2\int_{\varphi_i=0}^{1}\int_{\varphi_j=0}^{1-\varphi_i} d\varphi_i\wedge d\varphi_j = 1$$

4 Whitney Elements

In this chapter we first derive a simplified formulation of a Whitney 2-form, that only uses positions of grid vertices, instead of hat function gradients. Our goal is to represent a dipole source using Whitney forms, so that we are able to compare results from a numerical experiment with an analytical solution. A dipole source is described by a position $\mathbf{x}_0$ and momentum $\mathbf{p}$ whereas a Whitney basis function has neither a specific position nor a direction associated with it. In this Chaper we address these problems and find a way to represent a current dipole as a linear combination of Whitney 2-forms. Further we describe how the right hand side vector $\mathbf{f}$ of the descrite finite element formulation is assembled, when the source was modelled using the Whitney approach.

4.1 Alternative Formulation

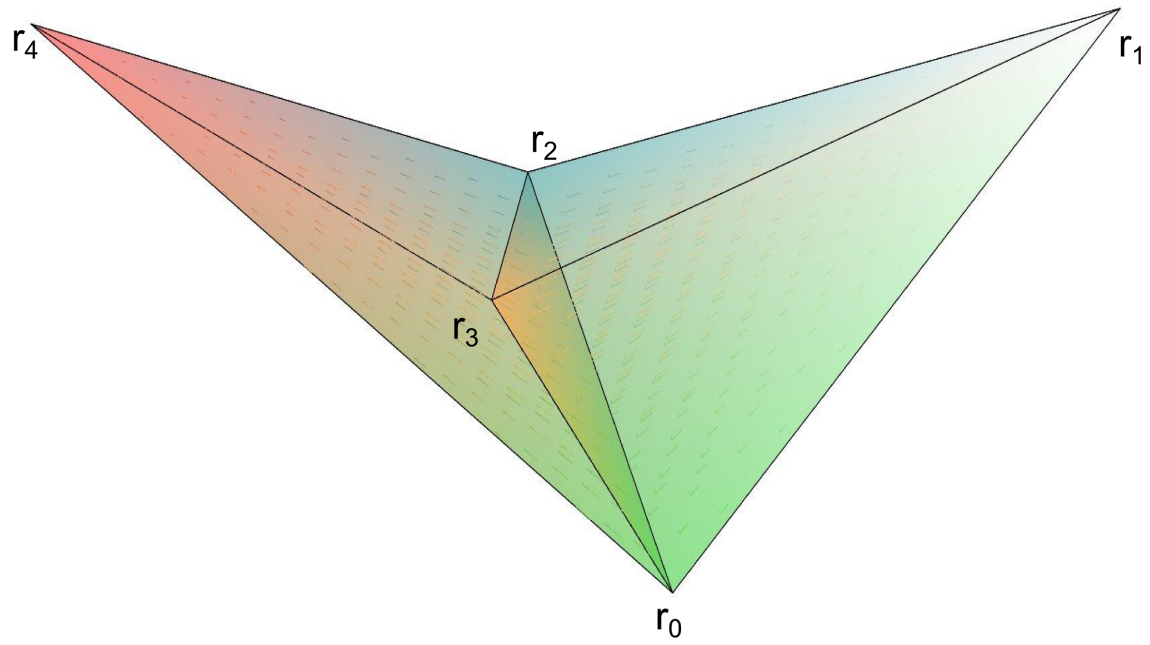

Figure 4.1 – Whitney Basis Function on two elements

In this section we will develop a simplified formulation of the Whitney basis which we will use later on to incorporate Whitney elements into the finite element method. Therefore we assume tetrahedrons as depicted in 4.1. We denote the left tetrahedron, that consists of the vertices $\mathbf{r}_0, \mathbf{r}_2, \mathbf{r}_3, \mathbf{r}_4$, as T_1 and the right tetrahedron, consisting of $\mathbf{r}_0, \mathbf{r}_1, \mathbf{r}_2, \mathbf{r}_3$, as T_2.

We use the general formula (3.10) to obtain an interpolation of a 2-form that has unit flux over face $(0, 2, 3)$, using the hat functions φ_i that are associated to the vertices $\mathbf{r}_i$:

$$\mathbf{w}_{023} = 2\ (\varphi_0(d\varphi_2 \wedge d\varphi_3) + \varphi_2(d\varphi_3 \wedge d\varphi_0) + \varphi_3(d\varphi_0 \wedge d\varphi_2))$$

Assuming an euclidean metric this can be expressed with gradients and the cross product:

$$\mathbf{w}_{023} = 2\ (\varphi_0(\nabla\varphi_2 \times \nabla\varphi_3) + \varphi_2(\nabla\varphi_3 \times \nabla\varphi_0) + \varphi_3(\nabla\varphi_0 \times \nabla\varphi_2)) \tag{4.1}$$

We will now develop a simpler formulation of the same basis function, that uses only vertex positions instead of barycentric coordinates. First we write down a vector field, that has a vanishing flux over all faces but on face $(0, 2, 3)$, and claim that it is the same as the Whitney 2-form. We model that vector field in a way, such that it has similar properties like the Whitney basis function and show afterwards, that both formulations are indeed the same.

$$\mathbf{w'}_{023}|_{T_1} = c_1 \cdot (\mathbf{x} - \mathbf{r}_4) \qquad \mathbf{w'}_{023}|_{T_2} = -c_2 \cdot (\mathbf{x} - \mathbf{r}_1) \qquad \text{with} \quad \mathbf{x} = (x, y, z)^T$$

From Fig. 4.2 one can see that the normal component s of $\mathbf{w'}$ is constant across the face. The flux is then given as $\Phi = s \cdot A_{023}$, with A_{023} being the area of the face.
The constants c_1 and c_2 have to be chosen such that the flux Φ over face $(0, 2, 3)$ has unit value. We compute the flux Φ_1 using $\mathbf{w}_{023}|_{T_1}$ and the flux Φ_2 using $\mathbf{w}_{023}|_{T_2}$ and normalize both.

$$\Phi_i = s_i \cdot A_{023} = c_i \cdot h_{T_i} \cdot A_{023} \qquad \text{for} \quad i = 1, 2$$

Here h_{T_i} denotes the height of the respective tetrahedron i.e. the distance of the opposing vertices $\mathbf{r}_4$ and $\mathbf{r_1}$ to the common face $(0, 2, 3)$.

$$\Phi_i \stackrel{!}{=} 1 \ \Rightarrow\ c_i = \frac{1}{h_{T_i} \cdot A_{023}} = \frac{1}{3 \cdot vol(T_i)}$$

In the last step the volume formula for tetrahedrons was used.

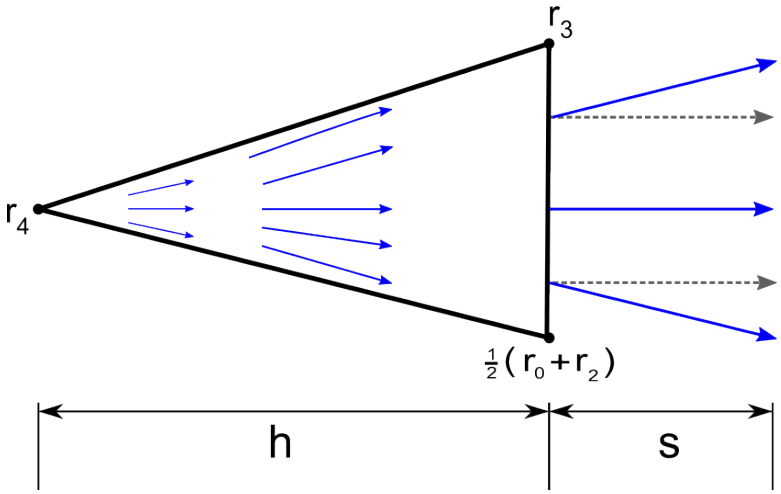

Figure 4.2 – Constant Normal Component of Whitney basis function

Substituting the c_i's back into the definition we get:

$$\mathbf{w'}_{023}|_{T_1} = \frac{1}{3 \cdot vol(T_1)} \cdot (\mathbf{x} - \mathbf{r_4}) \qquad \mathbf{w'}_{023}|_{T_2} = -\frac{1}{3 \cdot vol(T_2)} \cdot (\mathbf{x} - \mathbf{r_1}) \tag{4.2}$$

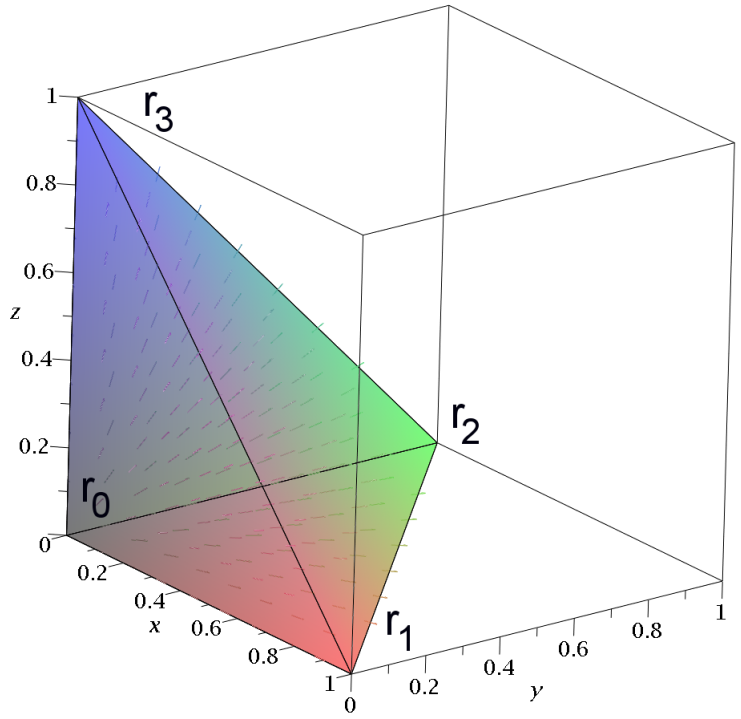

Figure 4.3 – Whitney Basis Function in Reference Element

The next step is, to show that both formulations $\mathbf{w}$ and $\mathbf{w'}$ are indeed the same. It is sufficient to show this on a reference element, because the results generalize by transforming both formulations with a bijective function, that maps the reference elements to arbitrary tetrahedrons. Our chosen reference element is depicted in Fig. 4.3. We use the Whitney basis function $\mathbf{w}_{123}$ with unit flux over face $(1, 2, 3)$

We start with the formulation coming from differential geometry:

$$\begin{aligned}\mathbf{w}_{123} &= 2\left(\varphi_1(\nabla\varphi_2 \times \nabla\varphi_3) + \varphi_2(\nabla\varphi_3 \times \nabla\varphi_1) + \varphi_3(\nabla\varphi_1 \times \nabla\varphi_2)\right) = \\ &= 2\left(x(\mathbf{e}_y \times \mathbf{e}_z) + y(\mathbf{e}_z \times \mathbf{e}_x) + z(\mathbf{e}_x \times \mathbf{e}_y)\right) = \\ &= 2(x\mathbf{e}_x + y\mathbf{e}_y + z\mathbf{e}_z)\end{aligned}$$

and can see that it is indeed the same as the simplified formulation (4.2).

$$\mathbf{w'}_{123} = \frac{1}{3 \cdot vol(T_2)} \cdot (\mathbf{x} - \mathbf{r_0}) = 2\mathbf{x} = 2(x\mathbf{e}_x + y\mathbf{e}_y + z\mathbf{e}_z) \tag{4.3}$$

4.2 Mean Direction of Ansatz function

In the last section we normalized our Whitney basis function, such that it had unit flux over its associated face (4.2). Our goal is to represent a dipole with an arbitrary position and direction using a combination of Whitney ansatz functions. Therefore we have to assign a direction to $\mathbf{w}_k$. We follow [PSCP11] and use the mean value $\mathbf{q}_k := \int_\Omega \mathbf{w}_k \, dV$ as direction.
In the strict sense a Whitney basis function must have unit flux over its associated face. However for further caculations it is more convenient to renormalize them, such that their mean direction $\mathbf{q}_k$ has unit length. Therefore we compute now $\mathbf{q}_k$ with the flux Φ as free parameter.

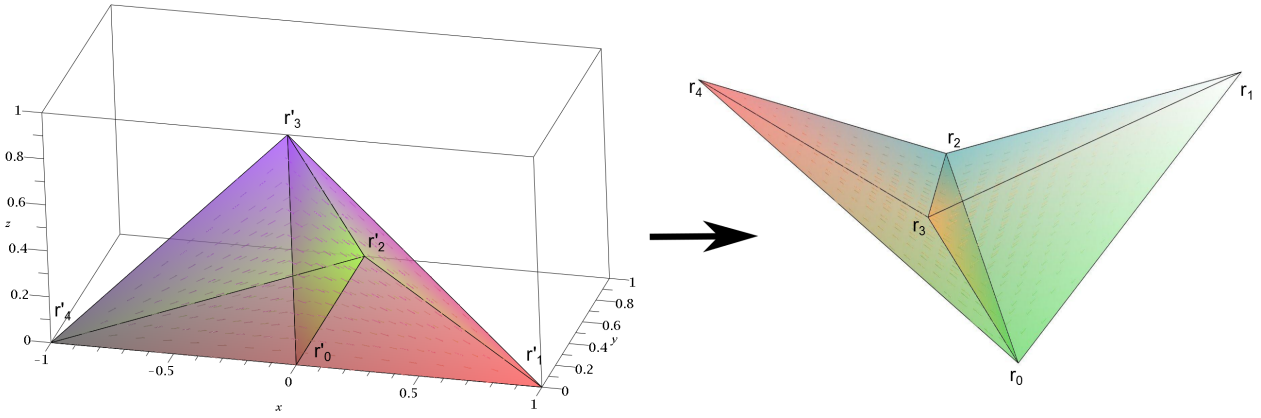

Figure 4.4 – Mapping reference elements to arbitrary tetrahedrons

First we write down (4.2) again, but now with an arbitrary flux Φ:

$$\mathbf{w'}_{023}|_{T_1} = \frac{\Phi}{3 \cdot vol(T_1)} \cdot (\mathbf{x} - \mathbf{r_4}) \qquad \mathbf{w'}_{023}|_{T_2} = -\frac{\Phi}{3 \cdot vol(T_2)} \cdot (\mathbf{x} - \mathbf{r_1}) \qquad (4.4)$$

One basis function has non-zero values on two tetrahedrons. To calculate the integral over one basis function we use two reference elements (Fig. 4.4).

$$\int_\Omega \mathbf{w}_k \, dV = \int_{T_1} \mathbf{w}_k \, dV + \int_{T_2} \mathbf{w}_k \, dV$$

Then we define mappings from these reference elements to general tetrahedrons: The first function ϑ_1 maps the right reference tetrahedron ($\mathbf{r'}_0$,$\mathbf{r'}_1$,$\mathbf{r'}_2$,$\mathbf{r'}_3$) to an arbitrary tetrahedron with vertices $\mathbf{r}_0$ up to $\mathbf{r}_3$. The primed position denote vertices in the reference elements, unprimed positions in the general tetrahedrons.

$$\vartheta_1(\mathbf{x}) = \begin{pmatrix} \vdots & \vdots & \vdots \\ (\mathbf{r}_1 - \mathbf{r}_0) & (\mathbf{r}_2 - \mathbf{r}_0) & (\mathbf{r}_3 - \mathbf{r}_0) \\ \vdots & \vdots & \vdots \end{pmatrix} \cdot \mathbf{x} + \mathbf{r}_0 = \mathbf{M}_1 \cdot \mathbf{x} + \mathbf{r}_0$$

$$\mathbf{r}_i = \vartheta_1(\mathbf{r'}_i) \quad \text{for} \quad i = 0, 1, 2, 3$$

Then the same is done for the left reference tetrahedron:

$$\vartheta_2(\mathbf{x}) = \begin{pmatrix} \vdots & \vdots & \vdots \\ -(\mathbf{r}_4 - \mathbf{r}_0) & (\mathbf{r}_2 - \mathbf{r}_0) & (\mathbf{r}_3 - \mathbf{r}_0) \\ \vdots & \vdots & \vdots \end{pmatrix} \cdot \mathbf{x} + \mathbf{r}_0 = \mathbf{M}_2 \cdot \mathbf{x} + \mathbf{r}_0$$

$$\mathbf{r}_i = \vartheta_2(\mathbf{r'}_i) \text{ for } i = 0, 2, 3, 4$$

With these transformations, the integrals can be rewritten to now go over the reference elements using the functional determinant of the transformations ϑ:

$$\int_{T_1'} \varphi_1(\mathbf{w}_k) \det(D\vartheta_1)\, dV + \int_{T_2'} \vartheta_1(\mathbf{w}_k) \det(D\vartheta_2)\, dV$$

$$-\frac{\Phi}{3 \cdot vol(T_1)} \int_{x=0}^{1} \int_{y=0}^{1-x} \int_{z=0}^{1-x-y} \mathbf{M}_1\mathbf{x} - \mathbf{r}_1 + \mathbf{r}_0\, dV + \frac{\Phi}{3 \cdot vol(T_2)} \int_{x=0}^{1} \int_{y=0}^{1+x} \int_{z=0}^{1+x-y} \mathbf{M}_2\mathbf{x} - \mathbf{r}_4 + \mathbf{r}_0\, dV$$

The determinants of $\mathbf{M}_1$ and $\mathbf{M}_2$ are the volumes of the parallelepiped spanned by their column vectors, which is the double of the tetrahedron volume.

Evaluating both integrals and simplifying yields:

$$\mathbf{q}_k = \int_\Omega \mathbf{w}_k\, dV = \frac{\Phi}{4}(\mathbf{r}_1 - \mathbf{r}_4) \tag{4.5}$$

For the basis function to have a mean direction of unit length we have to choose the flux as

$$\Phi = \frac{4}{||\mathbf{r}_1 - \mathbf{r}_4||} \tag{4.6}$$

4.3 Interpolation Methods

If we want to simulate a dipole pointing in an arbitrary direction $\mathbf{p}$, we have to use multiple Whitney basis functions. The task is to find a linear combination of ansatz functions $\sum c_k\, \mathbf{w}_k$ such that the flux distribution represents a given current dipole, at position $\mathbf{x}_0$ and dipole moment $\mathbf{p}$, as best as possible.

We use only basis functions that belong to faces of the tetrahedron where the current dipole is located. So we have four basis functions available, one for every face. Then we express the dipole moment as a linear combination of the basis function directions $\mathbf{q}_k$ and solve for the coefficients c_k. We have chosen the $\mathbf{w}_k$ such that $\mathbf{q}_k$ has unit length.

$$\mathbf{p} = \sum_{k=1}^{4} c_k \mathbf{q}_k$$

This is equivalent to the matrix equation:

$$\mathbf{Q} \cdot \mathbf{c} := \begin{pmatrix} | & | & | & | \\ \mathbf{q}_1 & \mathbf{q}_2 & \mathbf{q}_3 & \mathbf{q}_4 \\ | & | & | & | \end{pmatrix} \begin{pmatrix} c_1 \\ c_2 \\ c_3 \\ c_4 \end{pmatrix} \stackrel{!}{=} \mathbf{p}$$

Moore Penrose Pseudo Inverse

The matrix consisting of the $\mathbf{q}_k$ as column vectors is a 3x4 matrix and therefore the solution set is one dimensional, for non degenerate tetrahedrons. To solve this underdetermined equation system, one can use the Moore Penrose Pseudo Inverse which computes the minimum norm solution. When using this approach we effectively solve the following optimization problem:

$$\begin{aligned} &\text{minimize} && ||\mathbf{c}||_2 \\ &\text{subject to} && \mathbf{Q} \cdot \mathbf{c} = \mathbf{p} \end{aligned}$$

One major drawback of the above approach is, that we do not use the information, where exactly the current dipole is located inside the tetrahedron. We have used the current dipole position $\mathbf{x}_0$ only to choose which set of $\mathbf{w}_k$ to use, but the position inside the tetrahedron didn't enter the calculation. Instead of picking the minimum norm solution, we can incorporate the position information into the optimization problem.

Optimization approach

We reformulate the optimization problem using weights ω_k for each Whitney basis function:

$$\begin{aligned} &\underset{\mathbf{c}}{\text{minimize}} && \sum_{k=1}^{4} c_k^2 \, \omega_k \\ &\text{subject to} && \mathbf{Q} \cdot \mathbf{c} = \mathbf{p} \end{aligned} \tag{4.7}$$

In the weights ω_k we can encode additional information, that favors or penalizes a certain $\mathbf{w}_k$. A Whitney basis function has no definite position, but is spread out over two tetrahedrons. Nevertheless we can assign a position $\mathbf{r}_k^{\text{whi}}$ to $\mathbf{w}_k$. Possible positions are for example the center of the defining face, or the midpoint between the vertices that are not part of the defining face. In Section 5.2.1 we will analyze four possible candidates for $\mathbf{r}_k^{\text{whi}}$, and choose one that represents the Whitney basis function best.
To incorporate the dipole position $\mathbf{x}_0$ into the optimization problem we use the weights (4.8). These weights favor basis functions whose $\mathbf{r}_k^{\text{whi}}$ lies near the dipole position.

$$\omega_k = ||\mathbf{r}_k^{\text{whi}} - \mathbf{x}_0||_2^2 \tag{4.8}$$

Instead of weighting depending on the spatial distance, we can also choose weights that measure the angular distance between $\mathbf{w}_k$ and $\mathbf{p}$:

$$\omega_k = \cos^{-1}\left(\frac{\mathbf{p}}{||\mathbf{p}||} \cdot \mathbf{q}_k\right) \tag{4.9}$$

Both choices will be evaluated in terms of their accuracy in Section 5.2.3.

To solve the optimization problem, we first determine two special solutions of the equation system. This can be done by solving the system two times with an added 4th row, that has a 1 on the diagonal an 0 elsewhere. On the dipole direction vector $\mathbf{p}$ we also append a 4th row, with two arbitrary but different values. We solve the system for these two right hand sides and obtain two solutions $\mathbf{s}_1$ and $\mathbf{s}_2$. Then we express the solution space in a parametrized form:

$$\boldsymbol{\alpha}(\lambda) := \mathbf{s}_1 + \lambda(\mathbf{s}_2 - \mathbf{s}_1) =: \mathbf{a} + \lambda\mathbf{b} \tag{4.10}$$

This simplifies the optimization problem to:

$$\underset{\lambda}{\text{minimize}} \quad \sum_{k=1}^{4} \alpha_k(\lambda)^2\, \omega_k = \sum_{k=1}^{4} (a_k + \lambda b_k)^2\, \omega_k \tag{4.11}$$

We solve this by setting the first derivative with respect to λ to zero:

$$\frac{d}{d\lambda}\left(\sum_{k=1}^{4} (a_k + \lambda b_k)^2\, \omega_k\right) = 0$$

Solving for λ yields:

$$\lambda = \frac{\sum_{k=1}^{4} a_k b_k \omega_k}{\sum_{k=1}^{4} b_k^2 \omega_k}$$

Then we insert the computed value for λ into (4.10) and obtain a solution for the coefficient vector $\mathbf{c}$.

4.4 Whitney to Nodal Basis Transfer

Up to now we have shown, how a dipole source can be represented in a basis consisting of face based Whitney ansatz functions. However, for the finite element formulation we use a nodal basis, so a basis transformation is required to map between both formulations. This is done by basis transfer matrix $G \in \mathbb{R}^{NxF}$ where N is the number of nodes and F the number of faces.
We start with the weak formulation of the EEG forward problem (2.6). We assume a discretization of the potential $\psi_h = \sum_i \varphi_i \cdot u_i$ in the nodal (Lagrangian) basis, where φ_i denotes the hat function associated with node i. We discretize the primary current $\mathbf{J}^p$ using 2-forms, which means that we prescribe the flux for all faces on the mesh $\mathbf{J}^P = \sum_k c_k \mathbf{w}_k$. The summation index k runs over all faces of the mesh. [PSCP11]
We insert this representation into (2.10):

$$f(w) := \int_\Omega \mathbf{J}^P \cdot \nabla w \; dV = \int_\Omega \sum_k \mathbf{w}_k \cdot \nabla w \; dV$$

The right hand side vector $\mathbf{f}$ is then given as:

$$f_i = \sum_k c_k \int_\Omega (\nabla \cdot \mathbf{w}_k)\, \varphi_i \; dV \tag{4.12}$$

Using a the basis transformation matrix G, equation (4.12) can be written as $f = Gc$ where the vector c contains the Whitney coefficients c_i and the matrix G is defined as:

$$g_{ik} := -\int_\Omega (\nabla \cdot \mathbf{w}_k)\ \varphi_i\ dV$$

To calculate the entries of G, we map them again to the reference elements (Fig.4.4) where they have the simple formulation (4.4). We first note that the divergence of a Whitney basis function is constant and has the value:

$$\nabla \cdot \mathbf{w}_k = \frac{\Phi}{vol(T)}$$

We now have to distinguish two cases. First we look at $i = 0, 2, 3$ where the vertex v_i belongs to the common face (Fig. 4.1)

$$g_{ik} = \int_\Omega (\nabla \cdot \mathbf{w}_k)\ \varphi_i\ dV = \frac{\Phi}{vol(T_1)} \int_{T_1} \varphi_i\ dV - \frac{\Phi}{vol(T_2)} \int_{T_2} \varphi_i\ dV \qquad \text{for } i = 0, 2, 3$$

Using the fact that the integral of a nodal basis function x_i over one element T is $\frac{vol(T)}{4}$ we obtain:

$$g_{ik} = \frac{\Phi}{vol(T_1)} \frac{vol(T_1)}{4} - \frac{\Phi}{vol(T_2)} \frac{vol(T_2)}{4} = 0 \qquad \text{for } i = 0, 2, 3$$

In the second case $i = 1, 4$ the integrand is non-zero only on one element and the terms do not cancel out as in the previous case. Here we get:

$$g_{4k} = -g_{1k} = \frac{\Phi}{4}$$

Choosing the flux such that the mean direction of the Whitney ansatz function has unit length (4.6) the local basis transfer matrix has the following entries:

$$g_{ik} = \begin{cases} 0 & \text{for } i = 0, 2, 3 \\ ||\mathbf{R}_1 - \mathbf{R}_4||^{-1} & \text{for } i = 4 \\ -||\mathbf{R}_1 - \mathbf{R}_4||^{-1} & \text{for } i = 1 \end{cases} \tag{4.13}$$

4.5 Hexahedral Mesh

So far we've derived a source model for tetrahedral meshes, based on the theory of differential geometry and Whitney's interpolation method for 2-forms. Now we transfer this principle to hexahedral meshes. In the following we only look at the special case of meshes that consist entirely of cubes that are aligned along the coordinate axes. All results generalize to arbitrary hexahedral meshes by mapping the integration region of the axis aligned cube to a general hexahedron.

For developing face based ansatz functions we use the two reference hexahedrons depicted in 4.5. The length's in x,y and z direction are labeled as a_1,a_2,b and c as labeled in the figure. We denote the left hexahedron as C_1, the right as C_2.

A faced based ansatz function is required to have unit flux over the common face, and zero

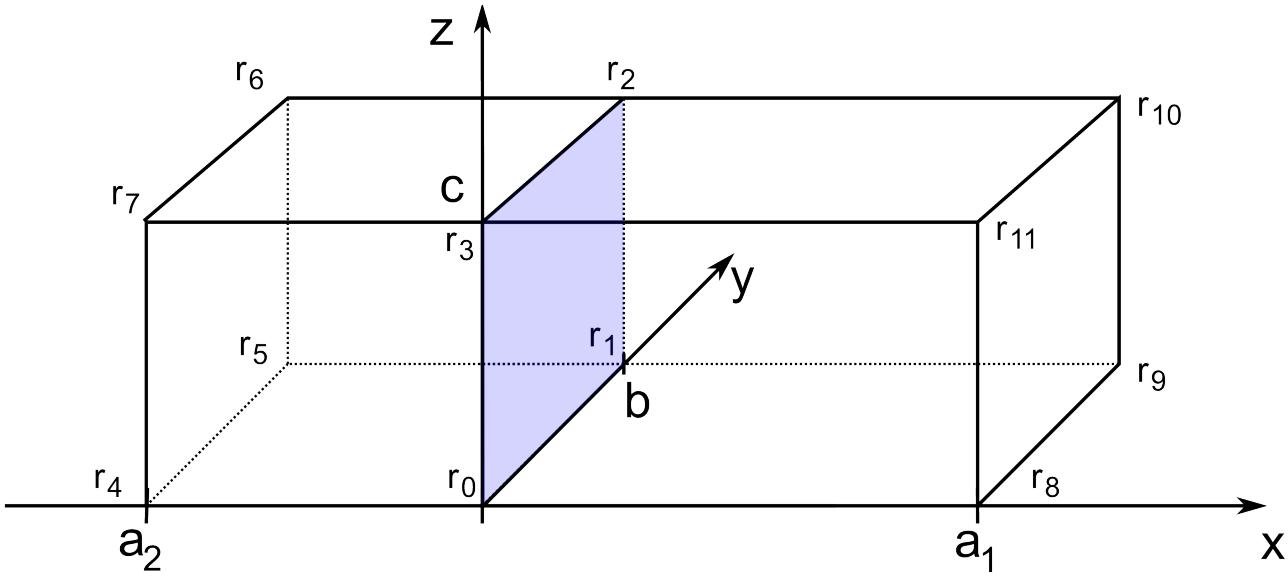

Figure 4.5 – Two reference hexahedrons

flux over all other faces. Furthermore the normal component on the common face has to be continuous.

One simple function that fulfills above properties is the following:

$$\mathbf{w}|_{C_1} = s\left(1 - \frac{x}{a_1}\right)\vec{e}_x \qquad \mathbf{w}|_{C_2} = s\left(1 + \frac{x}{a_2}\right)\vec{e}_x$$

where s denotes the length of the normal component on the common face.

Again we want to normalize the basis function such that the integral over its support yields a vector of unit length:

$$\vec{e}_x \cdot \int_{C_1 \cup C_2} \mathbf{w}\, dV \stackrel{!}{=} 1$$

$$s = \frac{2}{(a_1 + a_2) \cdot bc}$$

Now we can compute the coefficients of the basis transfer matrix g_{ik}. Due to symmetry the coefficients g_{ik} for $i = 0..3$ are equal. We will do a short calculation to determine g_{0k}. Therefore we need the bilinear ansatz function φ_0 for the vertex v_0:

$$\varphi_0|_{C_1} = \left(1 + \frac{x}{a_1}\right)\left(1 - \frac{y}{b}\right)\left(1 - \frac{z}{c}\right) \qquad \varphi_0|_{C_2} = \left(1 - \frac{x}{a_2}\right)\left(1 - \frac{y}{b}\right)\left(1 - \frac{z}{c}\right)$$

As in the tetrahedral case, coefficients that belong to the common face are zero:

$$\int_{C_1 \cup C_2} (\nabla \cdot \mathbf{w})\varphi_0\, dV = -\frac{n}{a_1}\int_{C_1} \varphi_0\, dV + \frac{n}{a_2}\int_{C_2} \varphi\, dV = -\frac{n}{a_1} \cdot \frac{a_1 bc}{8} + \frac{n}{a_2} \cdot \frac{a_2 bc}{8} = 0$$

For the other vertices the coefficients can be calculated similarly and yield:

$$g_{ik} = \begin{cases} +\frac{nbc}{8} = +\frac{1}{4(a_1+a_2)} & \text{for } i = 4,5,6,7 \\ -\frac{nbc}{8} = -\frac{1}{4(a_1+a_2)} & \text{for } i = 8,9,10,11 \end{cases}$$

We could have chosen more elaborate ansatz functions, that model the source more like a cylinder instead of a cube and has more flux towards the center of the cube:

$$\mathbf{w}|_{C_1} = n\left(1 - \frac{x}{a_1}\right)(y-b)(z-c)yz\ \vec{e}_x \qquad \mathbf{w}|_{C_2} = n\left(1 + \frac{x}{a_2}\right)(y-b)(z-c)yz\ \vec{e}_x$$

These choices would lead after normalization and integration to the same coefficients at the corner vertices.

5 Results

In this chapter we compare the previously shown source models, first on tetrahedral, then on hexahedral meshes.

5.1 Test Setup

5.1.1 Finite Element Meshes

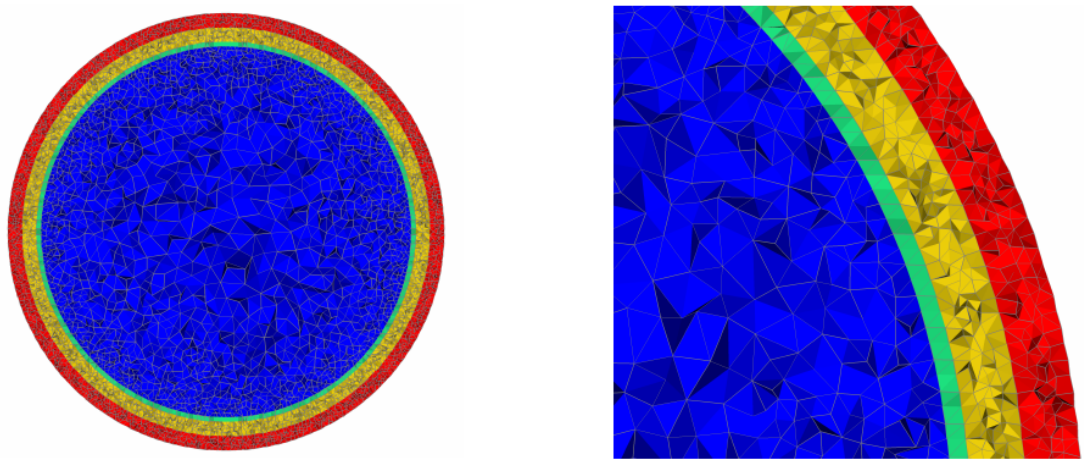

Figure 5.1 – Tetrahedral mesh of a sphere used for validation

For all the following numerical experiments, we use spherical meshes and compared the simulation results to the analytical solution obtained as described in Section 2.2.3. We used two different meshes for validation, one tetrahedral and one hexahedral mesh.
The tetrahedral mesh (Fig. 5.1) consists of approximately $5 \cdot 10^6$ elements and $8 \cdot 10^5$ vertices. It was generated by the software `tetgen` , which uses a *Constrained Delaunay Tetrahedralization* (CDT) approach [ST06]. For this mesh a volume constraint was set, such that each tetrahedron has at most a volume of 0.9 mm^3. This leads to a uniform tetrahedralization of the volume of the sphere.
The second test grid, is a hexahedral mesh, built out of axis aligned cubes, where each cube has an edge length of 1 mm. This results in a mesh with $3,2 \cdot 10^6$ elements and $3,3 \cdot 10^6$ nodes. Each mesh is divided into 4 compartments, modelling the scalp, skull, cerebrospinal fluid and brain tissue. Every compartment has a different conductivity (Table 5.1), that was chosen isotropic for all test cases. For the choice of the compartment dimensions and the conductivities we followed [LWA+09, MGB+98].

Compartment	Scalp	Skull	CSF	Brain
Outer shell radius (mm)	92	86	80	78
conductivity (S/m)	0.33	0.0042	1.79	0.33

Table 5.1 – Parametrization for the isotropic four-layer sphere meshes

5.1.2 Statistical Evaluation Method

In order to analyze the numerical errors it is common to simulate sources of different eccentricity, and plot the error as a function of the source eccentricity. Eccentricity here is defined as the ratio of the source radius to the radius of the innermost layer i.e. a source at the sphere center has an eccentricity of 0% whereas a source on the boundary between brain tissue and CSF has an eccentricity of 100% . Typically the numerical errors grow with growing eccentricity.
To evaluate the results of our numerical experiments, we use a statistical approach suggested by [Vor11]. In most previous studies the test sources all lie on a ray, starting at the midpoint of the model. For each eccentricity one sample was computed. As it turns out, the local mesh geometry has a significant influence on the error. Moving a source around inside a single element changes the error, some dipole models perform better when the source is positioned near a vertex, some when the source lies near the center of the tetrahedron. To avoid this effect, we simulate multiple sources per eccentricity and examine statistical properties of that sample.
For the accuracy analysis we will use two types of diagrams. The first type is called *box-plot* and shows the minimum, maximum and median for each eccentricity. The maximum and minimum are indicated by the upper and lower error bars, whereas the box shows the upper and lower quartile of the error. The black dash inside the box marks the error's median value.
The second plot type shows only the arithmetic mean of the error for all dipoles with the same radius as a line plot.
Simulations were done for radial and tangential dipole moments, where the tangential dipole moments were also chosen randomly.

5.1.3 Error Measures

The result of the discretized EEG Forward Problem is a vector, containing the potential at each node of the FEM mesh. In a realistic scenario, however, we are only interested in the potential at the electrodes at the surface of the domain. To do a realistic evaluation of the error we use an artificial electrode cap consisting of evenly spaced electrodes on the outermost sphere surface. For the tetrahedral mesh we used an electrode cap with 748 electrodes, the electrode cap for the hexahedral mesh had 134 electrodes. To obtain the potential at electrode positions, the *SimBio* software searches for the FEM node nearest to the electrode and uses that potential. The output of one simulation run is then a vector u_{sim}, where each entry represents one electrode potential. To evaluate the result we then compute the analytical solution for each electrode and put them in the vector u_{ana}.
To compare these two vectors, we have three different error measures available:

$$\text{RE}(u_{\text{ana}}, u_{\text{sim}}) := \frac{\|u_{\text{ana}} - u_{\text{sim}}\|_2}{\|u_{\text{ana}}\|_2} \tag{5.1}$$

$$\mathrm{RDM}(u_{\mathrm{ana}}, u_{\mathrm{sim}}) := \left\| \frac{u_{\mathrm{ana}}}{\|u_{\mathrm{ana}}\|_2} - \frac{u_{\mathrm{sim}}}{\|u_{\mathrm{sim}}\|_2} \right\|_2 \tag{5.2}$$

$$\mathrm{MAG}(u_{\mathrm{ana}}, u_{\mathrm{sim}}) := \frac{\|u_{\mathrm{sim}}\|_2}{\|u_{\mathrm{ana}}\|_2} \tag{5.3}$$

The relative error RE does not distinguish between topographic and magnitude errors. To overcome this limitation the error measures RDM and MAG are widely used [LWA+09, Vor11]. The relative distance measure RDM is invariant under scaling of each of its arguments, and thus only measures topographic errors. It can attain values between 0 and 2 with zero as the optimal value. The magnitude error MAG compares the length of its two inputs, by calculating the fraction of their norms. Note that in the optimal case when $u_{\mathrm{sim}} = u_{\mathrm{ana}}$ the MAG attains a value of 1.
In the following, we will use the combination of RDM and MAG to show the topography and magnitude error separately.

5.2 Tetrahedral Mesh

5.2.1 Associating a Position to Whitney Ansatz Function

To evaluate the performance of the Whitney dipole model, we have to compare simulation results to the analytical solution. However the analytical solution is only available for mathematical dipoles as right hand side. As described above, the mathematical dipole is a Dirac delta function multiplied by the dipole moment vector $\mathbf{p}$ and has therefore a definite position, whereas the support of a whitney basis function consists out of two tetrahedrons. To compare results obtained from these two models, we have to assign positions and moments to Whitney basis functions.
As we have described in Section 4.3, we use as dipole moment $\mathbf{p}$ the mean direction of the ansatz function $\mathbf{q}_k = \int_\Omega \mathbf{w_k}\, dV$. Up to now, we have left open the position $\mathbf{r}_k^{\mathrm{whi}}$ that represents $\mathbf{w}_k$ best.
We determine this position by doing numerical experiments, evaluating the error at a collection of positions that where suggested by [PSCP11]. These positions are linear combinations of the vertex positions of two adjacent tetrahedrons:

$$\sum_{i=1}^{5} \alpha_i \cdot \mathbf{r}_i$$

with $\mathbf{r}_i$ being the position vectors of the two tetrahedron as labeled in Fig. 5.2 The α_i's were chosen as listed in Table 5.2 .
Our tests were done in the following way: we pick out a Whitney basis function with unit mean direction ($||\mathbf{q}_k||_2 = 1$), i.e. we prescribe the flux over one triangle and run a simulation. Then we compare the outcome to the theoretical solution of a dipole source with position (A-D) and dipole moment $\mathbf{p} = \mathbf{q}_k$.
As can be seen in 5.3, position D achieves both the smallest MAG and RDM error for all tested eccentricities, which confirms the results from [PSCP11]. In the following, we will therefore

Location	α_1	α_2	α_3	α_4	α_5
A	1/3	1/3	1/3	0	0
B	1/5	1/5	1/5	1/5	1/5
C	1/9	1/9	1/9	1/3	1/3
D	0	0	0	1/2	1/2

Table 5.2 – Candidates for source location [PSCP11]

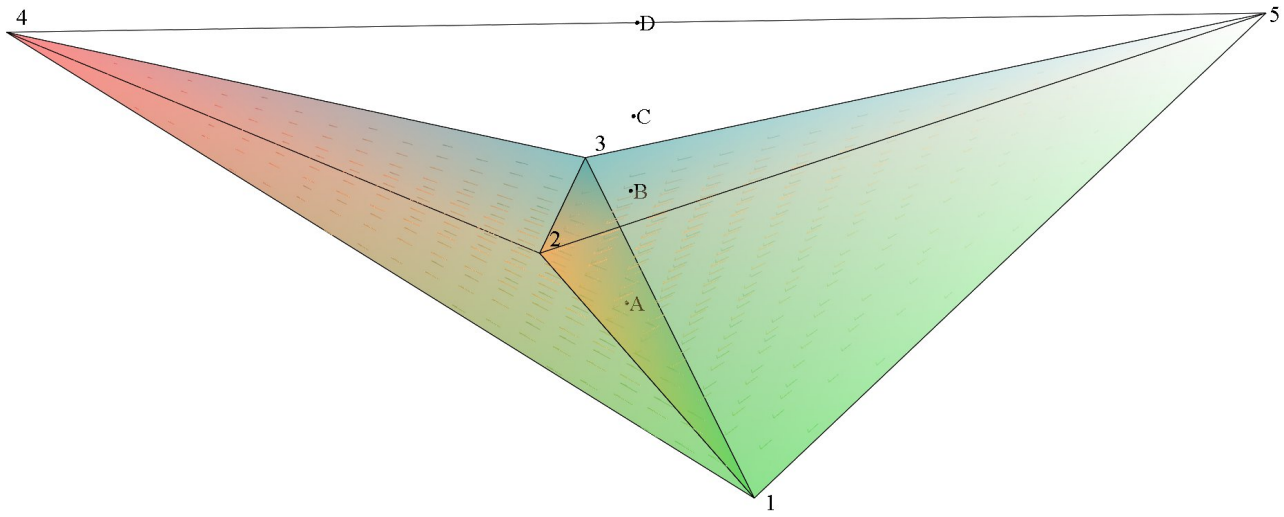

Figure 5.2 – Plot of whitney basis functions with source location candidates

use location D as associated position of a Whitney basis function. We will need this position for the direction interpolation scheme, described in Section 4.3.

5.2.2 Comparison without Interpolation

In the following testruns we want to investigate the numerical errors of the Whitney ansatz compared to other available dipole models. We pick one Whitney basis function and compute the dipole that best represents this function. As dipole moment we use the mean direction $\mathbf{q}_k$, and as position $\mathbf{x_0}$ the location (D) that showed the smallest errors in the previous tests.
Using these dipole parameters as input for the other dipole model would result in an unfair comparison, since we use optimal positions and directions for the Whitney model and arbitrary positions for the other dipole models. Therefore we first test which source configurations are well suited for the other models, so that we can evaluate all models under conditions where they perform best. In the following we use two types of plots: the first type shows the error distribution on a cross-section of a tetrahedral element. The axes show the barycentric coordinates λ_1 and λ_2 of the tetrahedron. The third coordinate λ_3 was fixed to a value of 0.1, so the cross-section is near a tetrahedron face and parallel to it.
The second plot type shows the errors of one dipole model as a function of the eccentricity. For every eccentricity we tested sources that were moved to the next vertex, to next element

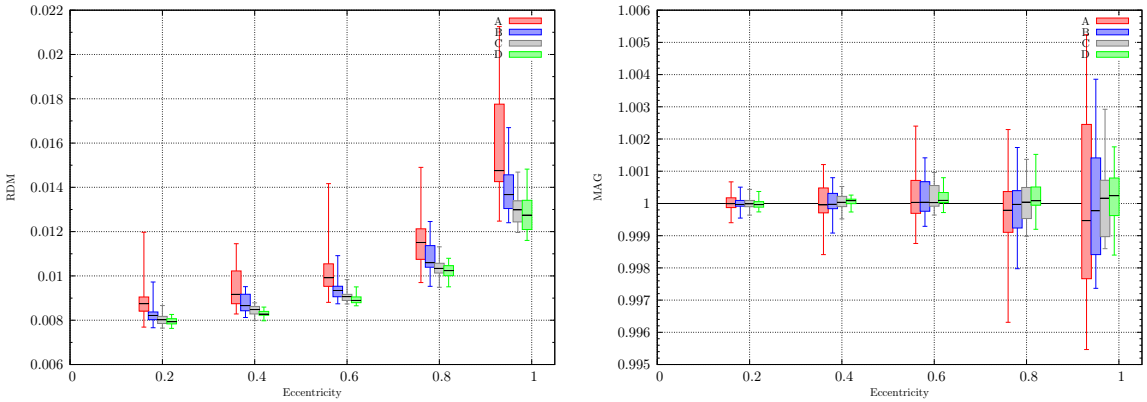

Figure 5.3 – RDM and MAG for Positions A-D

center, and sources that were not changed ("No Adaptation").
Figure 5.4 shows these two plots for the Venant dipole model. The closer the source is moved to a grid node, the smaller the errors become. This is true independent of the eccentricity.

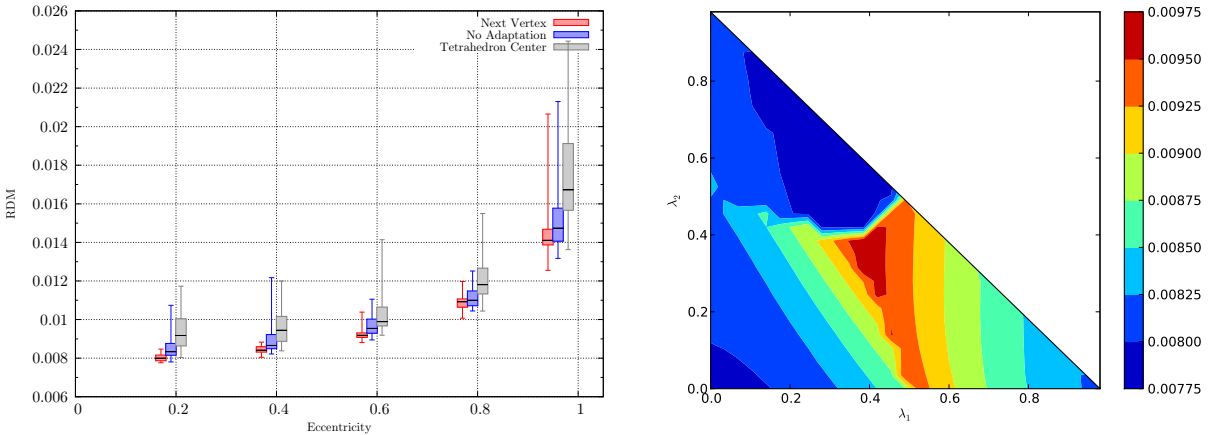

Figure 5.4 – RDM Error distribution inside an element for Venant Model

For the Partial Integration approach, the opposite is true. It favors positions that lie near element centers.
Since the Subtraction approach removes the source singularity on the right hand side analytically, there is no special position inside an element, where the errors are significantly smaller. In the following comparisons we also use sources at the element center to evaluate the Subtraction approach.
Having seen the errors of the different methods inside on element, we now compare all source models in the following way: For every eccentricity we generated random sources on the shell with the corresponding radius. Then we adapt the sources differently for each source model: For the Venant model we move the source to the next vertex, for the Partial Integration and Subtraction method we move them to the nearest tetrahedron center and for the Whitney approach to the next location (D). The first comparison will be without using an interpolation

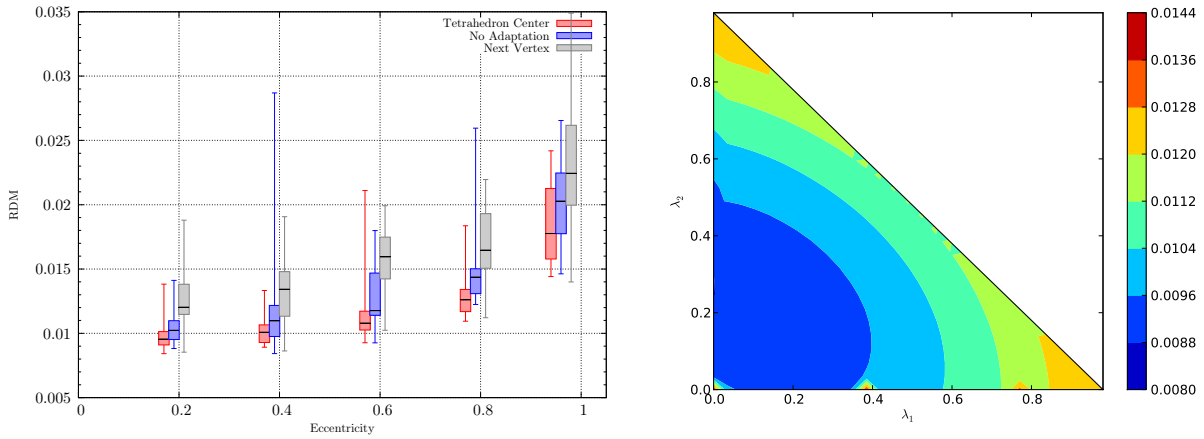

Figure 5.5 – RDM Error distribution inside an element for Partial Integration

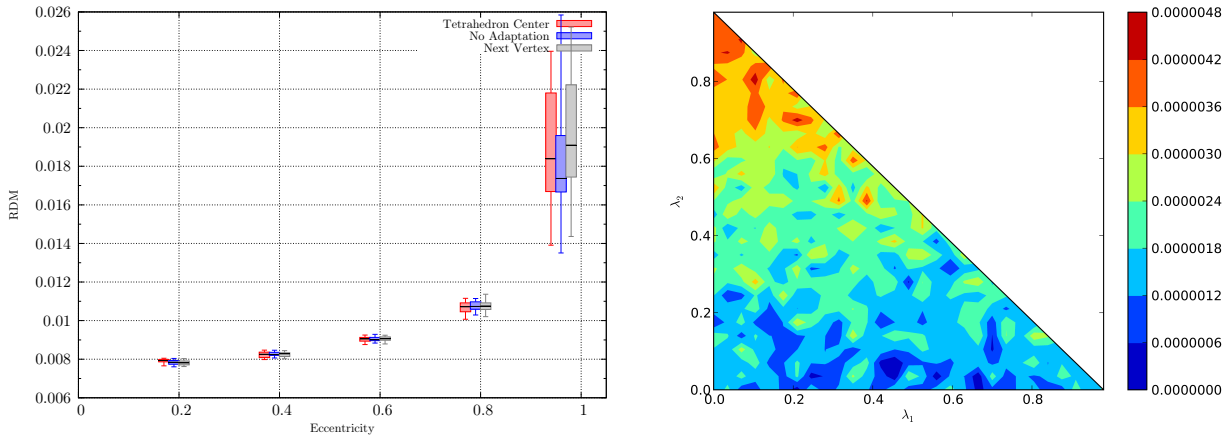

Figure 5.6 – RMD Error distribution inside an element for Subtraction

scheme in the Whitney approach, so we have to choose as dipole moment the mean direction of the Whitney ansatz function $\mathbf{p} = \mathbf{q}_k$. Note that this choice favors the Whitney ansatz, since no special directions can be chosen for the other models.

5.2.3 Interpolation Methods

The next step is to compare the different models using arbitrary source directions. Therefore we have to use the interpolation methods described in 4.3. There are three different methods available which we well evaluate with regard to their accuracy. The second method uses weights that are determined by the spatial distance between the source and the Whitney basis function. In section 4.3 we have left this position unspecified. Now that we have tested several positions (Fig. 5.2), we choose (D) since it represents the Whitney basis function best.
The accuracy of the three interpolation methods is shown in 5.8. We see that the interpolation scheme does not influence the accuracy very much, however the spatial interpolation method

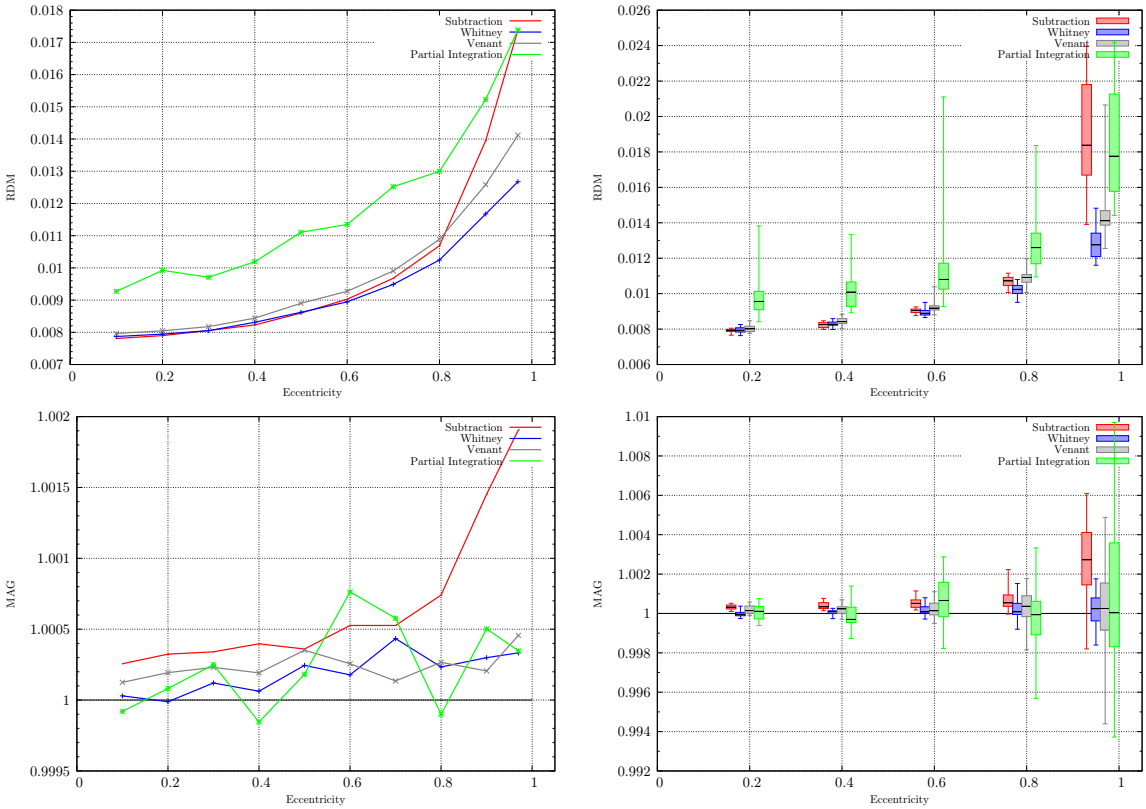

Figure 5.7 – Sources chosen such that they are optimal for each dipole model: Venant evaluated at vertices, Partial Integration at Subtraction at tetrahedron centers.

is slightly better than the others. Therefore we will use it for the next tests, which will involve arbitrary source directions.

5.2.4 Comparison with Interpolation

We did numerical experiments comparing all dipole models described above. The position and direction of the sources was chosen randomly and were not specially adapted to a certain model. As interpolation method for the Whitney model we used the optimzation approach with spatial weights (4.7). The results of these test runs are shown as eccentricity plots in Figure 5.9.

As we can see in Figure 5.9 the Whitney approach does not perform well in the general case, compared to the established models. Note that the Whitney approach has higher errors than the comparable direct Venant approach, which needs approximately the same computation time as we will see in section 5.4.

When using the Whitney dipole model the dipole positions and moments are discretized. This limitation was overcome by interpolation techniques which introduce additional errors. Therefore we did another set of test-runs, that use only positions and moments that are well suited for the Whitney model. To be able to do a fair comparison to the other models, we also have to evaluate them at conditions where they perform best.

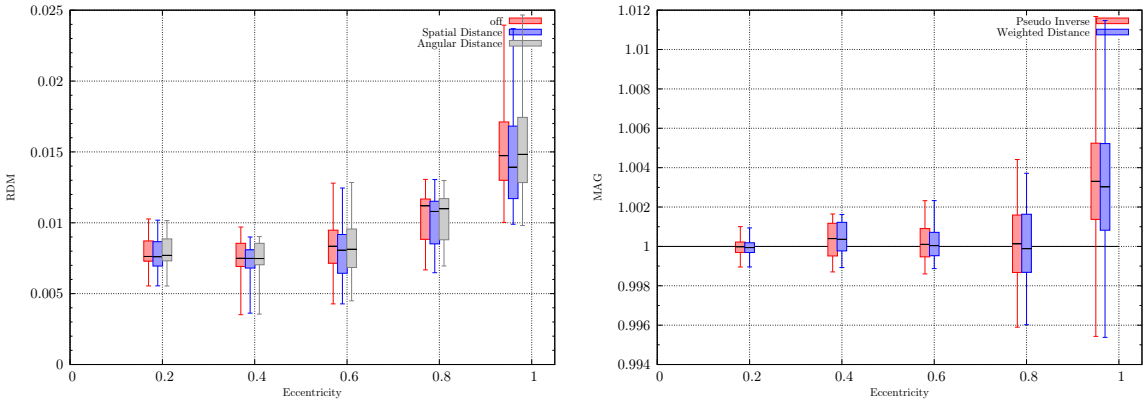

Figure 5.8 – Comparison of interpolation methods on tetrahedral mesh

5.3 Hexahedral Mesh

5.3.1 Comparing Whitney Ansatz to Analytical Model

A Whitney basis function is associated with a face, not a vertex, therefore it has no natural position associated to it. Since we have to compare analytical results, that can be calculated only for dipoles, with the numerical results obtained using the Whitney dipole model, we have to find a dipole position that best represents a given Whitney ansatz function. We've already done that in section 5.2.1 for tetrahedral elements, now we will do the same tests for hexahedral meshes.

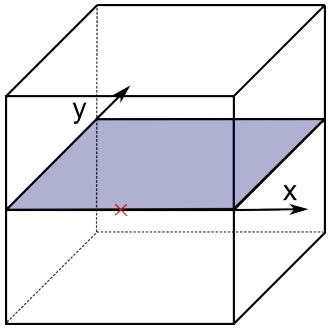

Figure 5.10 – Distribution of sources

Our test mesh consists out of axis aligned hexahedrons, that all have the same edge length. In this kind of mesh there is only one reasonable position that represents a Whitney basis function, and that is the midpoint of the related face. To confirm this assumption, we calculated the analytical solution for a grid of sources, located in a plane, that cuts the hexahedron in half (Fig. 5.10). As dipole moment we chose the direction orthogonal to the face (negative y direction). Then we compared these results to the result obtained using a Whitney basis function that belongs to the face $y = 0$. The red tag in Fig. 5.10 indicates the midpoint of that face.

The result of this comparison is shown in Fig. 5.11.

The plot confirms our guess: the smallest errors are on the plane $y = 0$. We have expected the error to be smallest for $x = 0.5$, however the smallest error is shifted to smaller x values. This is due to the position of the test hexahedron in the mesh: smaller x values of this element correspond to smaller eccentricities.

These results lead us to an algorithm, which can solve the forward problem for axis-aligned sources at arbitrary positions, using Whitney ansatz functions. Given a source at position $\mathbf{x}_0$ with an axis aligned moment $\mathbf{p} = \lambda \mathbf{e}_i$ ($\mathbf{e}_i$ denotes i'th euclidean basis vector), we use the Whitney ansatz function corresponding to the nearest face to $\mathbf{x}_0$, in $\mathbf{e}_i$ direction.

5.3.2 Comparison using Axis-Aligned Sources

We now compare this solution method for axis-aligned sources to the other dipole models. In the section about tetrahedral meshes, we have seen, that there are positions in the mesh were a given dipole model works particularly well. Sources at grid nodes suit the Venant approach whereas the Partial Integration method works better for sources at element centers. For the Whitney approach we choose sources that are located at the center of the associated face.
In the following plot (Fig. 5.12) we evaluate the performance of each dipole model, by using sources positions that are tailored to the specific model. Note that the dipole moments are still axis aligned, which benefits the Whitney approach. Because of this advantage the Whitney approach yields smaller errors than the other models.

5.3.3 Interpolation of Dipole Moment

We need to compute a solution for an arbitrary source direction $\mathbf{p} = \sum_i \lambda_i \mathbf{e}_i$, and we already have a method for computing the solution for a source $\lambda_i \mathbf{e}_i$. Due to the linearity of the forward problem we can build up a solution for an arbitrary source direction out of solutions of axis aligned sources. We do the same comparison again, but now for radial and tangential sources (Fig. 5.13), and see that the Whitney approach looses accuracy caused by the interpolation of the source direction.

5.4 Timing Measurements

Since the solution for the EEG forward problem is needed many times during an inverse computation, the solving process should be as fast as possible. The required runtime is an important aspect when choosing a dipole model. Therefore we compare the dipole models in this section, with respect to their computation times.
All measurements regarding performance were done on a standard notebook hardware. The test system was an Intel Core2 Duo CPU, operating at 2.5 GHz, with 5.8 GB of RAM.
We first have a look at the algorithm, used to obtain a potential at the EEG electrodes given a dipole source configuration. The typical procedure is, to first calculate the transfer matrix (Section 2.2.5) for a given geometry and conductivities, then run the simulation for S right hand sides at once. This procedure only makes sense if S is bigger than the number of electrodes, because otherwise it would be faster to calculate the solution directly, without using the transfer matrix. The computation of the transfer matrix is independent of the dipole model. Therefore we only look at the part of the algorithm, which changes when a different dipole model is used.
For the meshes used in our test cases, the transfer matrix is too big to be stored entirely in main memory. Consider the tetrahedral mesh that has approximately $N = 8 \cdot 10^5$ nodes, together with an electrode cap consisting of $E = 748$ electrodes. The transfer matrix has dimensions $N \times E$. Assuming that the entries are stored in *double* precision, together with a *double* size of 8 bytes the transfer matrix needs approximately 4.8 GB of storage. During the multiplication process, the transfer matrix is not entirely stored in main memory, but is read from the hard-disk row by row.
In order to speed up the multiplication, we assemble the right hand sides for all S source configurations beforehand, then read one row of the transfer matrix, compute the solution for

one electrode for all S sources and then read the next row. So the transfer matrix has to be loaded only one time, instead of S times. This approach is only possible for the direct source models (Venant, Partial Integration and Whitney). In these cases the right hand side vectors $\mathbf{f}$ are sparse, so there is not much space required to store all S right hand sides.
If the subtraction approach is used, this optimized calculation method is not possible. One reason is, that the right hand side vector of size N is not sparse any more. Additionally we have to store another full vector of size N, that holds the analytically computed solution ψ_0. If we would use the same method as for the direct methods, we would have to store $2 \cdot S$ non-sparse vectors of size N. We assume that S is big, at least bigger than E since then the transfer matrix approach would not be used. That means the storage for right hand sides would have to be twice as large as the storage of the transfer matrix. A trade-off has to be made between the number of stored right hand sides and multiple loading of the transfer matrix.
So we expect the subtraction approach to be slower than the other methods for multiple reasons. First the assembly of the right hand side itself is more compute intensive, since a numerical integration has to be done for each finite element to compute the term $\nabla \cdot (\sigma_{corr} \nabla u_0)$. The second reason is, that we have to deal with full right hand side vectors instead of sparse ones, which slows down the transfer matrix multiplication.
In the numerical experiment we calculated 300 sources and plotted the average time needed per source (Fig. 5.14). The left plot shows the runtimes for all source models, the right plot only the direct source models. The Whitney approach has a runtime comparable to the Venant approach. The most time expensive operations in the assembly of the right hand side, are queries for elements i.e. find an element given a source location. The runtime therefore depends mainly on the implementation of the mesh classes. The times for transfer matrix multiplication are more or less the same for all direct methods. These times only depend on the number of non-zero entries in the right hand side, which is approximately the same for all direct methods.
To summarize we note that all direct methods have approximately the same runtime, whereas the subtraction method is significantly slower.

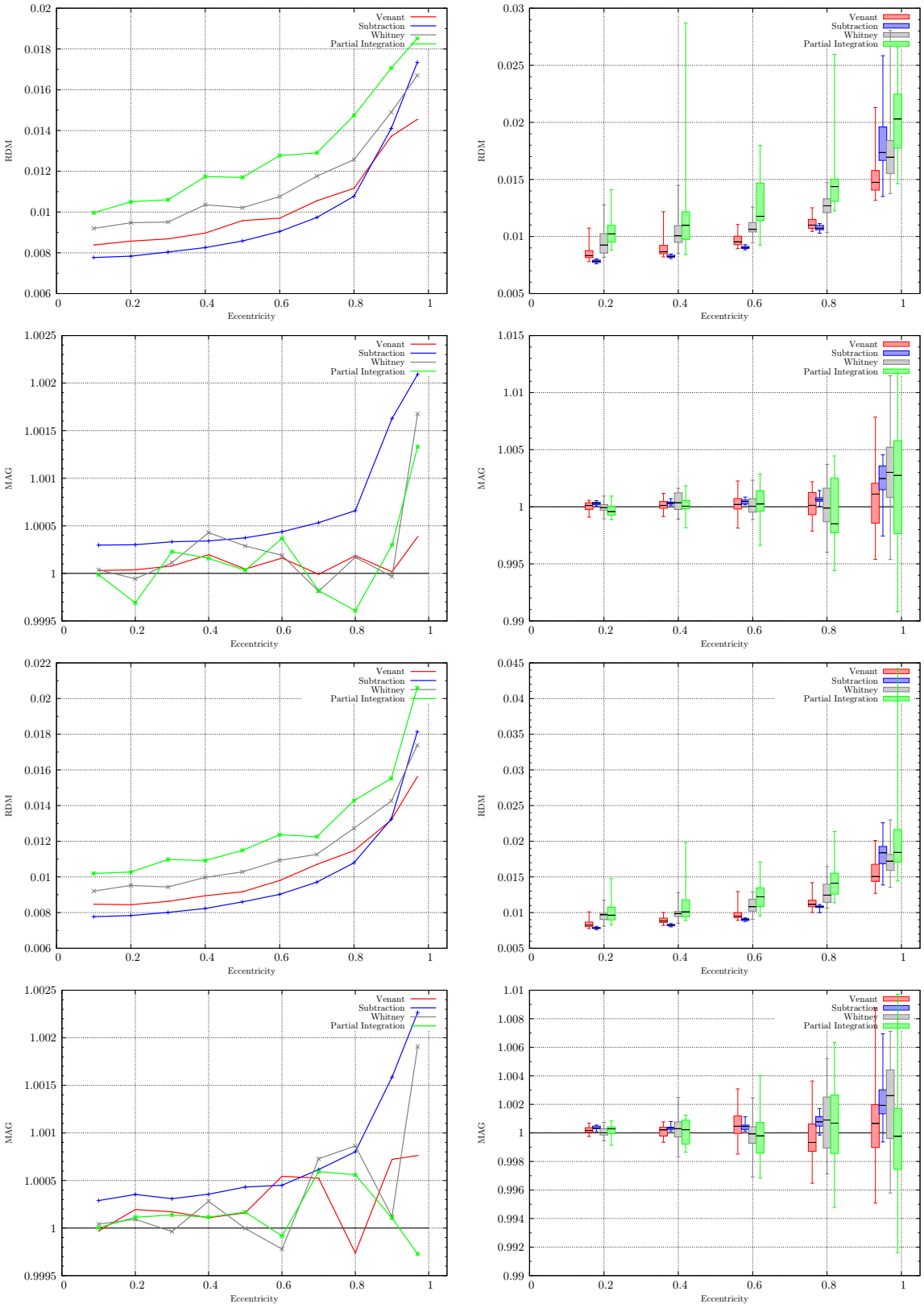

Figure 5.9 – Comparison of Dipole Models on tetrahedral mesh. The upper four plots were done using radial sources, the lower four using tangential sources. The right column shows the arithmetic mean of all measurements. The left column shows the same data as box-plots, where the x-values are slightly shifted for better readability. The maximal eccentricity is 97%

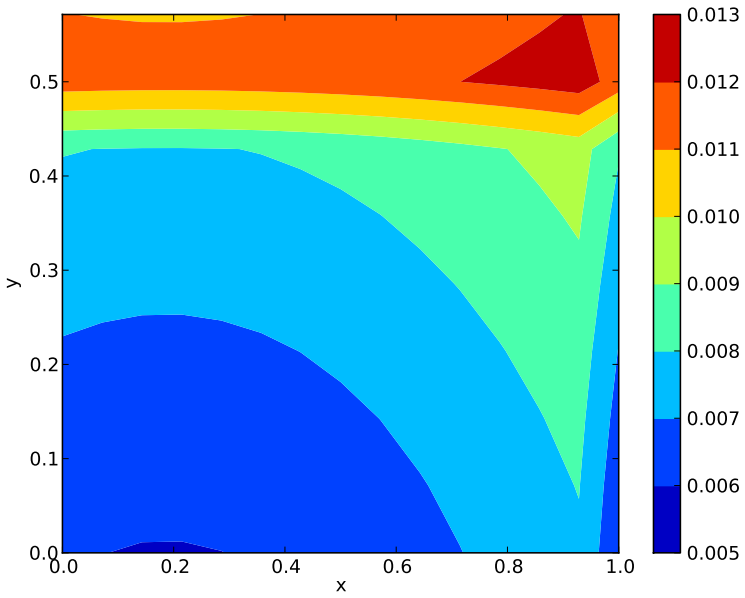

Figure 5.11 – RDM error of numerical solution, obtained by Whitney basis function at face $x = 0$, at different positions inside hexahedron

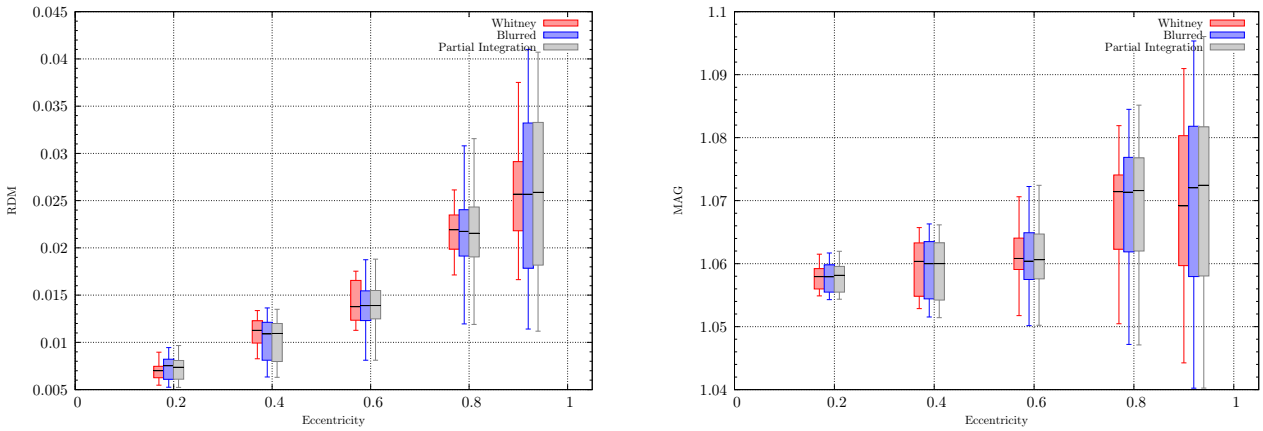

Figure 5.12 – RDM (left) and MAG (right) error for adapted source positions and axis-aligned directions on hexahedral mesh

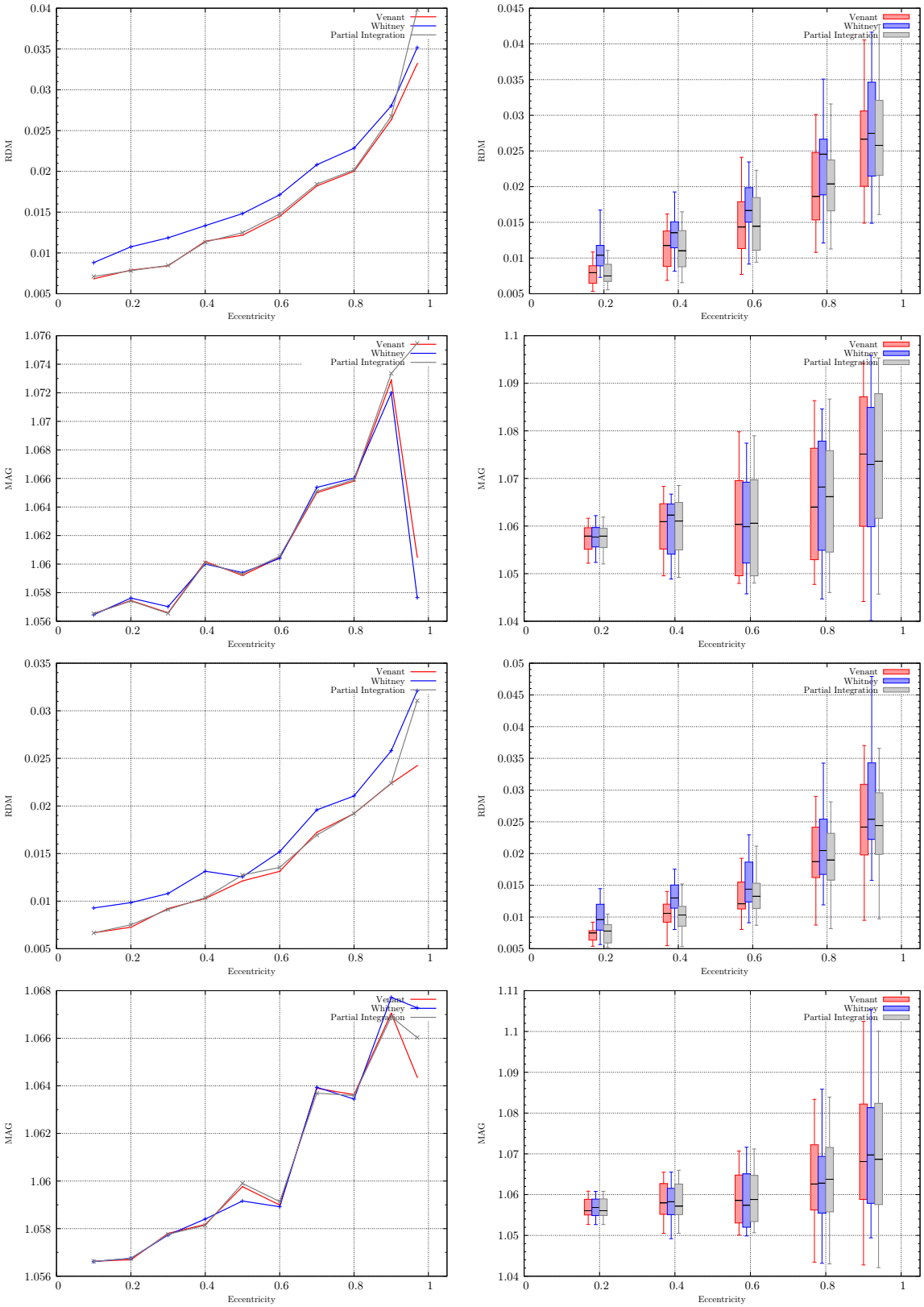

Figure 5.13 – Comparison of Dipole Models on hexahedral mesh. The upper four plots were done using radial sources, the lower four using tangential sources. The right column shows the arithmetic mean of all measurements. The left column shows the same data as box-plots, where the x-values are slightly shifted for better readability.

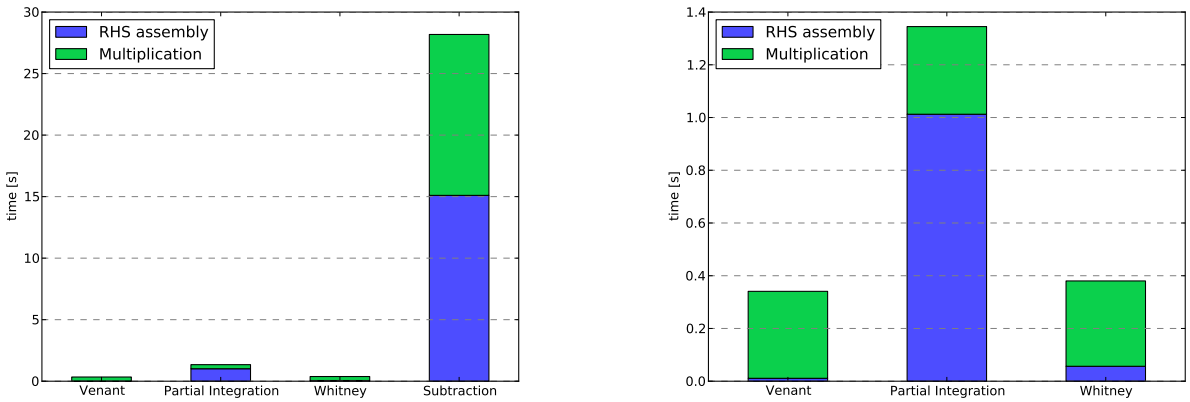

Figure 5.14 – Computation times for each dipole model

6 Conclusion

The major goals of the thesis where to

- extend the *SimBio* toolkit, such that it supports the Whitney source model,
- validate Whitney model using the analytical current dipole on spherical mesh, and to
- analyze the accuracy of the available source models on tetrahedral and hexahedral meshes

We have implemented a new type of source model, the Whitney model in the SimBio toolkit, that can be used to solve the EEG forward problem using the finite element method. First we discussed the theoretical background of Whitney forms, then showed how to incorporate the face based Whitney ansatz function in a finite element method that uses nodal basis functions. The implementation was validated using a spherical mesh, were a numerical solution exists for a current dipole. Therefore we had to represent a current dipole, consisting of a position and a dipole moment, as a combination of Whitney basis functions. We introduced three techniques that can be used to accomplish this.
In Chapter 5 we first investigated which dipole position represents a Whitney basis function best. The numerical experiments showed clearly that position (D) achieved the best results, confirming the findings of [PSCP11].
Afterwards different interpolation methods for the dipole moment were compared. Out of the three possible methods, the optimization approach that takes the dipole position into account, performed best and was used for further numerical measurements.
Using the previous findings, we then compared the four source models with respect to accuracy on tetrahedral and hexahedral meshes. In the first test we only used sources that can be represented as Whitney basis function without dipole moment interpolation. In this case the Whitney approach outperformed the other source models for high eccentricities. The second comparison involved sources with arbitrary dipole moment. In this general case the Whitney model was outperformed by the Venant and Subtraction approach.
Then the source models were tested with respect to their computation times. The runtime for all direct source models was approximately equal, whereas the subtraction approach took significantly longer, due to its indirect handling of the source singularity and the resulting non-sparseness of the right hand side.
To conclude we can say, that in terms of accuracy, the Whitney model outperforms other source models for special cases. In the general case however, different source models achieve higher accuracies. So an interesting topic for a future study could be the adaptation of the local mesh geometry to the direction of the source. Then the source can be represented as best as possible on the mesh and a high accuracy is achieved.

7 Bibliography

[BKF+97] H. Buchner, G. Knoll, M. Fuchs, A. Rienäcker, R. Beckmann, M. Wagner, J. Silny, and J. Pesch. Inverse localization of electric dipole current sources in finite element models of the human head. *Electroencephalography and clinical Neurophysiology*, 102(4):267–278, 1997.

[BS08] A.I. Bobenko and Y.B. Suris. *Discrete differential geometry: integrable structure*, volume 98. Amer Mathematical Society, 2008.

[DKT08] M. Desbrun, E. Kanso, and Y. Tong. Discrete differential forms for computational modeling. *Discrete differential geometry*, pages 287–324, 2008.

[DM88] JC De Munck. The potential distribution in a layered anisotropic spheroidal volume conductor. *Journal of applied Physics*, 64(2):464–470, 1988.

[DMVDS88] JC De Munck, BW Van Dijk, and H. Spekreijse. Mathematical dipoles are adequate to describe realistic generators of human brain activity. *Biomedical Engineering, IEEE Transactions on*, 35(11):960–966, 1988.

[DWD+09] F. Drechsler, CH Wolters, T. Dierkes, H. Si, and L. Grasedyck. A full subtraction approach for finite element method based source analysis using constrained delaunay tetrahedralisation. *NeuroImage*, 46(4):1055–1065, 2009.

[HHI+93] M. Hämäläinen, R. Hari, R.J. Ilmoniemi, J. Knuutila, and O.V. Lounasmaa. Magnetoencephalography—theory, instrumentation, and applications to noninvasive studies of the working human brain. *Reviews of modern Physics*, 65(2):413, 1993.

[KS05] J. Kaipio and E. Somersalo. *Statistical and computational inverse problems*, volume 160. Springer Verlag, 2005.

[LWA+09] S. Lew, C.H. Wolters, A. Anwander, S. Makeig, and R.S. MacLeod. Improved eeg source analysis using low-resolution conductivity estimation in a four-compartment finite element head model. *Human brain mapping*, 30(9):2862–2878, 2009.

[MGB+98] G. Marin, C. Guerin, S. Baillet, L. Garnero, and G. Meunier. Influence of skull anisotropy for the forward and inverse problem in eeg: simulation studies using fem on realistic head models. *Human Brain Mapping*, 6(4):250–269, 1998.

[MO06] S. Murakami and Y. Okada. Contributions of principal neocortical neurons to magnetoencephalography and electroencephalography signals. *The Journal of physiology*, 575(3):925, 2006.

[Moh04] M. Mohr. *Simulation of Bioelectric Fields: The Forward and Inverse Problem of Electro-encephalographic Source Analysis*. PhD thesis, Institut für Informatik der Technischen Fakultät der Friedrich-Alexander-Universität Erlangen-Nürnberg, 2004. Arbeitsberichte des Instituts für Informatik, Band 37.

[MP93] J.C. Munck and M.J. Peters. A fast method to compute the potential in the multisphere model. *IEEE transactions on biomedical engineering*, 40(11):1166–1174, 1993.

[MP95] J. Malmivuo and R. Plonsey. *Bioelectromagnetism: principles and applications of bioelectric and biomagnetic fields*. Oxford University Press, USA, 1995.

[Plo77] R. Plonsey. Action potential sources and their volume conductor fields. *Proceedings of the IEEE*, 65(5):601–611, 1977.

[PM99] R.D. Pascual-Marqui. Review of methods for solving the eeg inverse problem. *International Journal of Bioelectromagnetism*, 1(1):75–86, 1999.

[PSCP11] S. Pursiainen, A. Sorrentino, C. Campi, and M. Piana. Forward simulation and inverse dipole localization with the lowest order raviart—thomas elements for electroencephalography. *Inverse Problems*, 27:045003, 2011.

[ST06] H. Si and A. TetGen. A quality tetrahedral mesh generator and three-dimensional delaunay triangulator. *Weierstrass Institute for Applied Analysis and Stochastic, Berlin, Germany*, 2006. `http://tetgen.berlios.de`.

[Tao07] T. Tao. Differential forms and integration. Technical report, Tech. Rep., Department of Mathematics, UCLA, 2007.

[Vor11] Johannes Vorwerk. Comparison of Numerical Approaches to the EEG Forward Problem. Master's thesis, Universit"at M"unster, 2011.

[WABH07] C.H. Wolters, A. Anwander, G. Berti, and U. Hartmann. Geometry-adapted hexahedral meshes improve accuracy of finite-element-method-based eeg source analysis. *Biomedical Engineering, IEEE Transactions on*, 54(8):1446–1453, 2007.

[WAT+06] C.H. Wolters, A. Anwander, X. Tricoche, D. Weinstein, M.A. Koch, and RS MacLeod. Influence of tissue conductivity anisotropy on eeg/meg field and return current computation in a realistic head model: a simulation and visualization study using high-resolution finite element modeling. *NeuroImage*, 30(3):813–826, 2006.

[WGH04] C.H. Wolters, L. Grasedyck, and W. Hackbusch. Efficient computation of lead field bases and influence matrix for the fem-based eeg and meg inverse problem. *Inverse problems*, 20:1099, 2004.

[Whi57] H. Whitney. Geometric integration theory. *Princeton Press*, 1957.

[YNH91] Y. Yan, PL Nunez, and RT Hart. Finite-element model of the human head: scalp potentials due to dipole sources. *Medical and Biological Engineering and Computing*, 29(5):475–481, 1991.